Atmos. Chem. Phys., 24, 3953–3971, 2024
https://doi.org/10.5194/acp-24-3953-2024

Atmospheric Chemistry and Physics
Open Access
EGU

Chemical properties and single-particle mixing state of soot aerosol in Houston during the TRACER campaign

Ryan N. Farley[1,2], James E. Lee[3], Laura-Hélèna Rivellini[4], Alex K. Y. Lee[5], Rachael Dal Porto[6], Christopher D. Cappa[2,6], Kyle Gorkowski[3], Abu Sayeed Md Shawon[3], Katherine B. Benedict[3], Allison C. Aiken[3], Manvendra K. Dubey[3], and Qi Zhang[1,2]

[1]Department of Environmental Toxicology, University of California, Davis, CA 95616, USA
[2]Agricultural and Environmental Chemistry Graduate Group, University of California, Davis, CA 95616, USA
[3]Earth and Environmental Sciences Division, Los Alamos National Laboratory, Los Alamos, NM, USA
[4]Department of Chemistry, University of Toronto, Toronto, ON, Canada
[5]Air Quality Processes Research Section, Environment and Climate Change Canada, Toronto, ON, Canada
[6]Department of Civil and Environmental Engineering, University of California, Davis, CA 95616 USA

Correspondence: Qi Zhang (dkwzhang@ucdavis.edu)

Received: 11 October 2023 – Discussion started: 23 October 2023
Revised: 6 February 2024 – Accepted: 12 February 2024 – Published: 3 April 2024

Abstract. A high-resolution soot particle aerosol mass spectrometer (SP-AMS) was used to selectively measure refractory black carbon (rBC) and its associated coating material using both the ensemble size-resolved mass spectral mode and the event trigger single particle (ETSP) mode in Houston, Texas, in summer 2022. This study was conducted as part of the Department of Energy Atmospheric Radiation Measurement (ARM) program's TRacking Aerosol Convection interactions ExpeRiment (TRACER) field campaign. The study revealed an average ($\pm 1\sigma$) rBC concentration of $103 \pm 176\,\mathrm{ng\,m^{-3}}$. Additionally, the coatings on the BC particles were primarily composed of organics (59 %; $219 \pm 260\,\mathrm{ng\,m^{-3}}$) and sulfate (26 %; $94 \pm 55\,\mathrm{ng\,m^{-3}}$). Positive matrix factorization (PMF) analysis of the ensemble mass spectra of BC-containing particles resolved four distinct types of soot aerosol, including an oxidized organic aerosol ($\mathrm{OOA_{BC,PMF}}$) factor associated with processed primary organic aerosol, an inorganic sulfate factor ($\mathrm{SO_{4,BC,PMF}}$), an oxidized rBC factor ($\mathrm{O\text{-}BC_{PMF}}$), and a mixed mineral dust–biomass burning aerosol factor with significant contribution from potassium ($\mathrm{K\text{-}BB_{BC,PMF}}$). Additionally, *K*-means clustering analysis of the single-particle mass spectra identified eight different clusters, including soot particles enriched in hydrocarbon-like organic aerosol ($\mathrm{HOA_{BC,ETSP}}$), sulfate ($\mathrm{SO_{4,BC,ETSP}}$), two types of rBC, OOA ($\mathrm{OOA_{BC,ETSP}}$), chloride ($\mathrm{Cl_{BC,ETSP}}$), and nitrate ($\mathrm{NO_{3,BC,ETSP}}$). The single-particle measurements demonstrate substantial variation in BC coating thickness with coating-to-rBC mass ratios ranging from 0.1 to 100. The mixing state index (χ), which denotes the degree of homogeneity of the soot aerosol, varied from 4 % to 94 % with a median of 40 %, indicating that the aerosol population lies in between internal and external mixing but has large temporal and source type variability. In addition, a significant fraction of BC-containing particles, a majority enriched with oxidized organics and sulfate, exhibit sufficiently high κ values and diameters conducive to activation as cloud nuclei under atmospherically relevant supersaturation conditions. This finding bears significance in comprehending the aging processes of rBC-containing particles and their activation into cloud droplets. Our analysis highlights the complex nature of soot aerosol and underscores the need to comprehend its variability across different environments for accurate assessment of climate change.

1 Introduction

Soot aerosol, predominantly emitted from the incomplete combustion of fossil fuels and biomass, strongly absorbs solar radiation and contributes to positive climate forcing (Bond et al., 2013; IPCC, 2021; Ramanathan and Carmichael, 2008). The microphysical and optical properties of soot aerosol are profoundly influenced by the mixing state of black carbon (BC) and aerosol constituents internally mixed with BC (Cappa et al., 2012). The properties of ambient soot aerosol undergo dynamic variations during their aging processes in the atmosphere, such as the condensation of low-volatility or semi-volatile vapors, coagulation with preexisting aerosol, and heterogenous oxidation.

When freshly emitted, soot aerosol is often hydrophobic, but condensation of hygroscopic material, such as secondary organic aerosol (SOA) or inorganic salts, enables soot to act as cloud condensation nuclei (CCN) and alter cloud properties (Lambe et al., 2015; Motos et al., 2019; Wu et al., 2019; Zuberi et al., 2005). Additionally, the rate at which BC is scavenged by wet deposition, and therefore its atmospheric lifetime, is controlled by the hygroscopicity of its coating (Emerson et al., 2018; Yang et al., 2019). The presence of non-absorbing coating materials can also enhance aerosol light absorption through the so-called lensing effect, leading to disparities between optical models and observations (Cappa et al., 2012, 2019; Fierce et al., 2020; Lack and Cappa, 2010; Lee et al., 2022; Xie et al., 2019). The competition between the absorption enhancement and reduced lifetime from internal mixing of BC significantly affects its climate impacts and is not well understood (Hodnebrog et al., 2014).

Understanding the chemical and microphysical properties of soot aerosol and the complexities associated with its mixing state, which involves the interaction and incorporation of BC with other aerosol components, is crucial for comprehending its impact on the climate system and refining climate change assessment. Process level modeling studies with detailed mixing state treatments show that current simple model parameterizations can bias the climate forcing of BC (Fierce et al., 2017).

To address this problem, the present study investigates the intricate properties and dynamic variations of mixed soot particles with state-of-the-art chemical and microphysical instruments to determine their influence on cloud development in Houston, TX. This study is part of the U.S. Department of Energy (DOE)-sponsored TRacking Aerosol Convection interactions ExpeRiment (TRACER), which aims to unravel the interactions between clouds and aerosols in urban areas. Houston is a subtropical city heavily impacted by anthropogenic emissions from gasoline and diesel vehicles, cargo ships, and petrochemical industries (Al-Naiema et al., 2018; Bean et al., 2016; Schulze et al., 2018; Yoon et al., 2020). The abundance of soot particle sources and the high levels of photochemical activity in Houston make it an ideal location for studying urban soot aerosol characteristics and atmospheric processing.

Previous ambient measurements in Houston have reported average BC concentrations ranging between 0.31 and 0.80 $\mu g\,m^{-3}$ (Levy et al., 2013; Yoon et al., 2020). Additionally, a study utilizing ambient vapors within an environmental chamber in Houston found that after 18 h of atmospheric processing, monodisperse BC aerosol is transformed from a highly fractal morphology into spherical particles with a significant simultaneous increase in absorption enhancement (E_{abs}) (Peng et al., 2016). Another study by Levy et al. (2013) utilized measurements of BC aerosol effective density to probe the mixing state of soot particles in Houston and found that although the soot particles were often internally mixed with other species, an externally mixed BC population was also present during rush hour.

Despite the importance of soot aerosol at this site, detailed measurements of the composition and properties of BC-containing aerosol have not been performed in Houston. A particularly significant gap in knowledge pertains to the mixing states of soot aerosols. In this study, a soot particle aerosol mass spectrometer (SP-AMS) configured with only the laser vaporizer was used to selectively measure submicrometer particles (PM_1) containing black carbon. Additionally, a co-located dual-vaporizer SP-AMS, equipped with a $PM_{2.5}$ inlet, was deployed concurrently to provide measurements of the bulk $PM_{2.5}$ composition. Comprehensive measurements of aerosol optical properties were also collected to explore the effects of mixing state and coating composition on light absorption. Here, we report the results of ensemble and single-particle measurements of BC-containing aerosol and use them understand how size-resolved mixing leads to compositional differences between BC-containing and BC-free aerosols.

2 Methods

2.1 Sampling location and instrumentation

Measurements were performed at a U.S. Department of Energy (DOE)-managed site at the La Porte Municipal Airport (29.670° N, 95.058° W) from 28 June to 1 August 2022, as a part of the TRACER intensive operating period. The La Porte site is located approximately 30 km ESE of downtown Houston and is surrounded by residential and commercial areas (Fig. S1 in the Supplement). The Port of Houston and Houston Ship Channel (HSP) are located about 5 km to the northeast, and there are multiple refineries and other industrial and petrochemical plants located in the region. Although there was an active small aircraft runway nearby, we see no evidence of aircraft emissions impacting our measurements.

A suite of instrumentation for the comprehensive characterization of aerosol chemical and optical properties was housed in a temperature-controlled trailer owned by the Los Alamos National Laboratory (Fig. S1). Among them,

two high-resolution time-of-flight soot particle aerosol mass spectrometers (SP-AMS; Aerodyne Inc., Billerica MA.) were deployed simultaneously. One SP-AMS was operated in the laser-only configuration, allowing for the measurement of BC-containing PM_1, while the other SP-AMS incorporated both a laser and thermal vaporizer and a $PM_{2.5}$ aerodynamic lens system, aiming to characterize both BC-containing and non-refractory $PM_{2.5}$ (NR-$PM_{2.5}$) (Avery et al., 2020; Williams et al., 2013). Details of supporting instrumentation are provided in Sect. S1.1 in the Supplement.

2.2 Soot particle aerosol mass spectrometer (SP-AMS) operation and data analysis

2.2.1 SP-AMS measurement and data processing

The laser-only SP-AMS utilized in this study was modified by removing the tungsten thermal vaporizer in order to selectively detect particles containing black carbon. The SP-AMS is described in detail in previous publications (DeCarlo et al., 2006; Onasch et al., 2012). Briefly, ambient aerosols are sampled through an aerodynamic lens system and sorted based on their vacuum aerodynamic diameter (D_{va}) within the particle time-of-flight (PToF) chamber. A Nd:YAG intracavity (1064 nm) laser is utilized to selectively vaporize particles containing absorbing material, such as refractory black carbon (rBC). The resulting gaseous molecules are ionized using 70 eV electron impact ionization and measured using high-resolution time-of-flight mass spectrometry. The mass spectrometer was operated in the optical "V" mode with a mass resolution ($m/\Delta m$) of 2500 and was programmed to switch between three different sampling modes: the ensemble mass spectrum (MS) mode, the efficient particle time-of-flight (ePToF) size mode, and the event trigger single particle (ETSP) mode (DeCarlo et al., 2006; Onasch et al., 2012).

MS and ePToF measurements were analyzed in the SQUIRREL (v. 1.65C) and PIKA (v. 1.25C) analysis toolkits within the IGOR Pro (v. 8.04) environment, and concentrations were determined from the high-resolution peak fittings. Ambient rBC was quantified using the sum of C_1^+ to C_{10}^+. As the signal at C_1^+ can be influenced by both organics and rBC, the C_1^+ related to rBC was constrained using the ratio of C_3^+ to C_1^+ measured during the regal black calibration (0.65). The limit of detection (LOD) for each species was determined as 3σ during filtered air measurements when a HEPA filter was placed upstream of the SP-AMS. The LOD for 5 min averaging was 106, 17, 6, 11, 12, and 2 ng m^{-3} for organics, rBC, sulfate, nitrate, chloride, and ammonium, respectively. Additional details of SP-AMS operation and calibration are provided in Sect. S1.2.

2.2.2 Positive matrix factorization analysis of ensemble mass spectra

Source apportionment of the ensemble mass spectra was performed by positive matrix factorization (PMF) analysis using the PMF evaluation tool (PET) (Paatero and Tapper, 1994; Ulbrich et al., 2009). Organic and inorganic ions were included in the PMF matrix to reduce rotational ambiguity as well as to explore the distribution of inorganic species across the factors (Sun et al., 2012). This included HR organic ions between 12–120 amu, major ions related to rBC, sulfate, and nitrate, and UMR signal between m/z 121–307. PMF solutions up to 8 factors were assessed based on mass spectral and temporal features. Four meaningful factors were identified and include an oxidized organic aerosol factor ($OOA_{BC,PMF}$), an oxidized black carbon factor (O-BC_{PMF}), an inorganic sulfate factor ($SO_{4,BC,PMF}$), and a mixed biomass burning–mineral dust factor (K-$BB_{BC,PMF}$).

2.2.3 Event trigger single particle (ETSP) data processing and K-means clustering

The event trigger single particle mode was used to explore the mixing state of individual ambient particles, as done previously (Lee et al., 2019; Ma et al., 2023; Willis et al., 2019; Ye et al., 2018). The vaporization, ionization, and detection processes are identical to what is described above. However, rather than averaging the measured signals across all MS extractions, individual extractions (single-particle events) are identified and saved if the signal at predefined m/z values is above a set threshold. Table S1 shows the three regions of interest (ROIs), consisting of individual or a range of m/z values used to trigger particle events and the corresponding ion thresholds needed at each ROI. m/z 36 and 43 were selected to target rBC and OA, respectively. ROI 3 encompassed the total signal within the range of 46–150 amu, allowing for capturing particle events containing sulfate, nitrate, and/or high molecular weight organics. Note that the settings were altered slightly after the first week to better target OA.

The unit mass resolution (UMR) data were processed in Tofware v2.5.13 prior to inputting into the Cluster Input Preparation Panel (CIPP), a tool developed by Lee et al. (2015), to identify real particle events. For each event, the total ion signal was defined as the sum of all ions except for m/z 14 (N^+), 16 (O^+), 18 (H_2O^+ and $^{18}O^+$), 20 (Ar^{2+}) 28 (N_2^+), 32 (O_2^+), and 40 (Ar^+), as they are significantly influenced by air signal. A simplified fragmentation table using the same fragmentation ratios as those from the ensemble measurements (Allan et al., 2004) was used to quantify the contribution of different aerosol species. The minimum ion threshold was set as the average number of ions plus 3 standard deviations in the particle-free regions (defined as 10–50 and 2000–4000 nm), and any events falling below this threshold were discarded. Throughout the campaign, organized into 1-week segments, the minimum ion threshold

varied slightly, ranging between 21–27 ions. Additionally, events were considered valid if the signal of any individual species (rBC, sulfate, nitrate, chloride, potassium) exceeded the average plus 3 standard deviations of that species within the particle-free region.

In total, 14 699 single-particle events were identified and imported for K-means clustering. Clustering was performed within IGOR Pro v. 8.04 using the Cluster Analysis Panel (CAP) (Lee et al., 2015). Prior to clustering analysis, additional, noisy ions were removed including m/z 15 ($^{15}N^+$), 17 (NH_3^+, HO^+), 19 ($H_2^{18}O^+$), 22 (CO_2^{2+}), 182 ($^{182}W^+$), 183 ($^{183}W^+$), and 186 ($^{186}W^+$). Single-particle spectra were normalized to the total ion signal. Solutions up to 15 clusters were analyzed based on change in Euclidian distance as well as the spectral features, size distributions, and temporal patterns of each class (Fig. S2).

The chosen solution included 12 classes; however, clusters that showed similar features were merged for a more coherent representation (Fig. S3). Specifically, sulfate signal was found to be split between three different clusters: one predominantly comprising m/z 64 (SO_2^+), another featuring elevated m/z 48 (SO^+), and a third with elevated m/z 80 (SO_3^+) and 81 (HSO_3^+). Although these spectra may potentially hold intrinsic significance (e.g., aerosol acidity), it is more likely that this splitting behavior captures statistical variability in sulfate fragmentation. Consequently, these clusters were combined. Two OOA-like clusters were also identified, showing comparable size distributions and temporal trends. However, due to limitations in the UMR signal, it was not possible to discern meaningful differences between these clusters and they were combined. Finally, one cluster displayed signal spikes at seemingly random masses (m/z 76, 112, 130, 145), making it challenging to provide a physically meaningful interpretation. Given the limited occurrence of these events ($< 0.5\,\%$ of particle count), these spectra were assumed to be noise and were discarded from further analysis. NH_x^+ ions were not included in the particle clustering analysis; therefore, ammonium mass associated with each cluster was estimated assuming particle neutralization.

2.3 Quantification of aerosol mixing state and estimation of single-particle hygroscopicity

The aerosol mixing state was quantified using the metrics presented in Riemer and West (2013). The single-particle diversity (D_i) describes the number of chemical components in a single particle, weighted by the mass fraction of each component. The components used in this analysis were Org, rBC, sulfate, nitrate, chloride, and potassium. D_i varies from 1 when a particle is composed of only a single component to the total number of species (in this work 6) when every species composes equal mass fractions. D_i is calculated using the following formula:

$$D_i = \prod_{a=1}^{A} \left(p_i^a\right)^{-p_i^a}, \tag{1}$$

where p_i^a is the mass fraction of species a within particle i measured in the ETSP mode. The average single-particle diversity (D_α) is the weighted average of D_i across an aerosol population and is calculated as

$$D_\alpha = \prod_{i=1}^{N} (D_i)^{p_i}, \tag{2}$$

where p_i is the mass fraction of particle i in the population. D_γ measures the bulk population diversity and is calculated as

$$D_\gamma = \prod_{a=1}^{A} \left(p^a\right)^{-p^a}, \tag{3}$$

where p^a is the mass fraction of species a in the aerosol population measured in the ensemble mode.

While D_i and D_α were calculated based on the single-particle spectra from ETSP measurements, D_γ is a parameter derived from the ensemble measurements. As the ensemble MS and ETSP measurements were carried out sequentially at 20 min interval, hourly averages of D_α and D_γ were calculated to determine the mixing state index (χ). χ describes the degree of population homogeneity and varies from 0 %, signifying a fully external mixture, to 100 %, which indicates a fully internal mixture and is defined as

$$\chi = \frac{D_\alpha - 1}{D_\gamma - 1}. \tag{4}$$

The hygroscopicity of individual particles was predicted using the Zdanovskii–Stokes–Robinson (ZSR) mixing rule and the hygroscopicity parameter (κ) introduced in Petters and Kreidenweis (2007). Details of these calculations are given in Sect. S1.4 and S1.5.

3 Results

3.1 Overview of soot aerosol composition and properties in Houston during TRACER

3.1.1 Soot aerosol composition and diurnal variations

Meteorological conditions during TRACER were hot and humid, typical of summertime conditions at this subtropical site (Fig. S4). The average ($\pm 1\sigma$) temperature was $29 \pm 3\,°C$, and average RH was $72 \pm 13\,\%$ with strong diurnal variation. Throughout the measurement period there were several heavy precipitation events; however these rarely lasted longer than a few hours. The wind showed a consistent diurnal profile with weak ($< 2\,m\,s^{-1}$) southerly/southwesterly winds overnight and stronger ($> 5\,m\,s^{-1}$) southeasterly

winds in the afternoon (Fig. S5). This pattern is a result of a strong sea-breeze dynamic previously identified in the Houston area and results in the accumulation of local emissions overnight, followed by the advection of marine or processed air masses during the day (Banta et al., 2005; Caicedo et al., 2019; Li et al., 2020).

The average black carbon concentration was $0.10 \pm 0.18\,\mu g\,m^{-3}$, which is significantly lower than the average of $0.31 \pm 0.22\,\mu g\,m^{-3}$ measured in May 2009 (Levy et al., 2013) and $0.80 \pm 0.69\,\mu g\,m^{-3}$ measured in September 2013 (Yoon et al., 2020). However, both of those prior measurements were conducted at the University of Houston, which is closer to the urban core of Houston. The rBC concentration measured by the laser-only SP-AMS agrees well with a co-located SP2 (slope = 1.05, $r^2 = 0.67$, Fig. 1e) and the dual-vaporizer SP-AMS with a $PM_{2.5}$ inlet (slope = 1.14, $r^2 = 0.62$; Fig. S6). The slightly higher rBC concentration measured by the dual vaporizer SP-AMS may be due to additional rBC mass present in the 1–2.5 µm range. Additionally, the relationship between the SP-AMS rBC and the $PM_{2.5}$ aerosol absorption at 532 nm, determined using orthogonal distance fitting constrained to an intercept of 0, yields a slope of $13.8\,m^2\,g^{-1}$ ($r^2 = 0.46$). This value is higher than the expected mass absorption coefficient (MAC) of pure black carbon of $7.5 \pm 1.2\,m^2\,g^{-1}$ (Bond and Bergstrom, 2006; Liu et al., 2020) and can be explained by absorption from dust particles, absorbing material present between 1–2.5 µm or absorption enhancement due to BC mixing state (Cappa et al., 2012; Lack and Cappa, 2010). Further analysis of the aerosol optical properties will be included in a separate publication.

The diurnal pattern of rBC concentration shows a weak bimodal cycle, with higher concentrations seen in the morning and early afternoon and lower concentrations in the evening and overnight (Fig. 1a). The morning peak at 08:00 local time (LT) coincides with high gas-phase NO_x and CO concentrations and is likely related to fresh vehicle emissions during rush hour (Figs. 1a, S5). Due to the high boundary layer height in the afternoon (2–3 km), the increase of rBC between 16:00–17:00 LT is likely due to a combination of elevated vehicle emissions, industrial emissions, and the regional transport of BC-containing aerosol.

The soot aerosol coating thickness was estimated using the parameter $R_{coat\,/\,BC}$, calculated by taking the mass ratio of coating material to refractory black carbon. The term "coating material" is used to refer to the total inorganic and organic species found within the soot particles and does not imply knowledge of particle morphology or the coating being present as a layer on the black carbon core. Figure 2a presents the frequency of $R_{coat\,/\,BC}$ occurrences for the entire campaign. Each ensemble $R_{coat\,/\,BC}$ measurement represents the average mass ratio of all submicrometer soot particles sampled during the 5 min averaging period, while the $R_{coat\,/\,BC}$ calculated from the single-particle measurements represents the mass ratios for individual soot particles. The frequency histograms of $R_{coat\,/\,BC}$ display log-normal distributions for both the ensemble and single-particle measurements, but with substantially different median values of 4.5 and 1.5, respectively (Fig. 2a). The ensemble $R_{coat\,/\,BC}$ measurements agree well with previous measurements in urban areas, which typically vary between 1–10 (Collier et al., 2018; Healy et al., 2015; J. Wang et al., 2020). However, there were periods of thickly coated particles with $R_{coat\,/\,rBC}$ values exceeding 10, indicating that a portion of the soot aerosol at this site may have undergone extensive atmospheric processing or was emitted with an existing coating by a primary source such as biomass burning. The distribution of $R_{coat\,/\,BC}$ measured by ETSP highlights a population of nearly uncoated BC particles with $R_{coat\,/\,BC}$ less than 1, indicating substantial variation in the rBC mixing state. The diurnal profile of ensemble $R_{coat\,/\,BC}$ appears inversely related to the rBC concentration, with the lowest values occurring in the morning and afternoon (Fig. 1a). These time intervals are likely influenced by fresh, local emissions from vehicles or industrial sources, showing similar $R_{coat\,/\,BC}$ values to previous measurements taken near roadways (Lee et al., 2017). The soot aerosol coating is dominated by organic material (59 %) followed by sulfate (25 %) and ammonium (9 %) (Fig. 3a). Potassium contributes 3 % while nitrate and chloride each contribute 1 %. Figure 2 also shows the chemical composition of rBC coatings at different $R_{coat\,/\,BC}$ values, determined from both ensemble spectra (Fig. 2c) and single-particle spectra (Fig. 2d). Overall, as the $R_{coat\,/\,BC}$ ratio increases, the coating composition remains similar with a slight increase in the sulfate mass fraction, which is consistent with the formation of secondary aerosol upon atmospheric aging. Further details regarding the single-particle composition across varying $R_{coat\,/\,BC}$ values, along with insights into particle mixing states, are provided in the subsequent sections.

The diurnal cycle of Org_{BC} is similar to that of rBC and shows a slight morning increase (Fig. 1b). The diurnal profiles of both rBC and Org_{BC} show minima between 19:00 and 23:00 LT, indicating the transport of cleaner, marine air masses to the site. The $SO_{4,BC}$ profile shows little diurnal variation, highlighting its regional sources (Fig. 1c). The ratio of $SO_{4,BC}$ to rBC peaks between 20:00 and 23:00 LT possibly due to long-range transport of sulfate-rich aerosol. The observed $SO_{4,BC}$ concentration was unlikely to be significantly impacted by sea salt emissions, as the SP-AMS signals for $NaCl^+$, Cl^+ and HCl^+ were low despite these ions being detectable with the laser vaporizer if internally mixed with rBC. Instead, we hypothesize that $SO_{4,BC}$ is primarily attributed to ammonium sulfate formed from the oxidation of either marine-derived DMS or SO_2 from anthropogenic sources such as crude oil processing or other petrochemical industries (Ahmed et al., 2021; Rivera et al., 2010). We see little evidence for other forms of sulfate, such as methanesulfonic acid (MSA), primarily due to the absence of marker

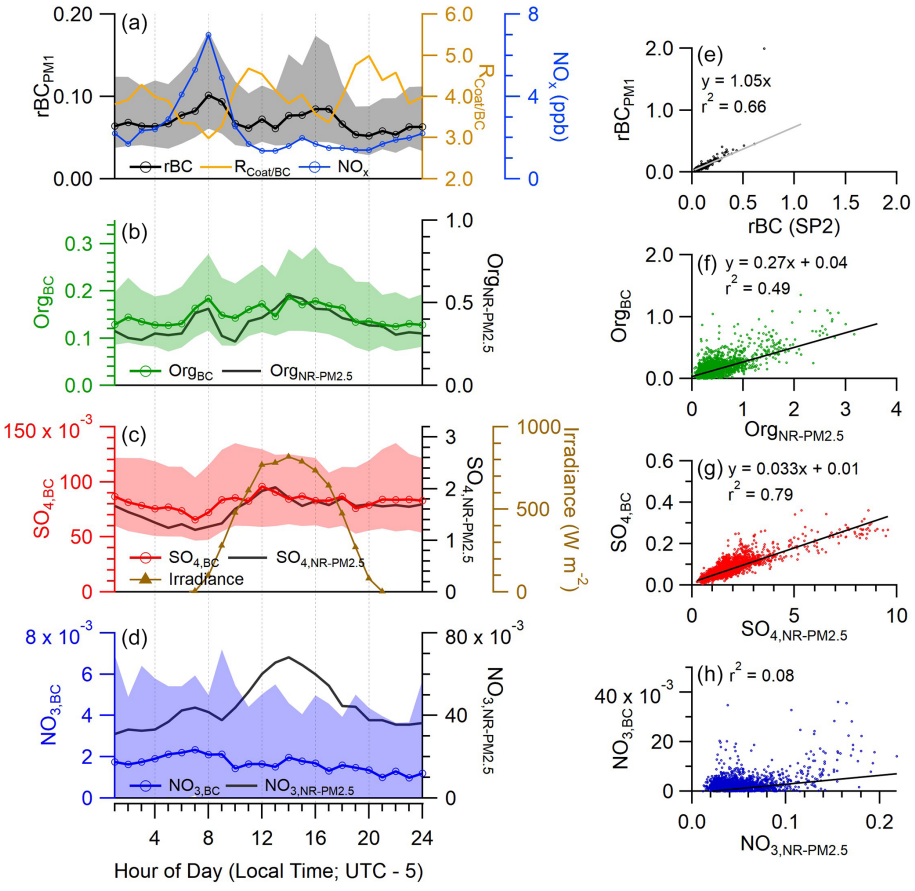

Figure 1. **(a)** Diurnal profile of rBC concentration, coating-to-rBC mass ratio ($R_{\mathrm{coat\,/\,BC}}$), and gas-phase NO_x. **(b–e)** Diurnal profile of aerosol species mixed with BC (colored traces with markers) and present in the NR-$PM_{2.5}$ fraction (black traces). Markers indicate the median, and shaded area indicates the interquartile range. **(e)** Correlation between rBC measured by SP-AMS and co-located SP2. **(f–h)** Scatterplot between species concentration present in BC fraction and NR-$PM_{2.5}$ fraction. Trend lines are orthogonal distance regression. All units are in $\mu g\,m^{-3}$, except for $R_{\mathrm{coat\,/\,BC}}$, which is a dimensionless value.

ions for MSA, such as $CH_3SO_2^+$ and $CH_4SO_3^+$ (Ge et al., 2012a).

Figure 1b–d also show the diurnal profiles of non-refractory $PM_{2.5}$ (NR-$PM_{2.5}$) collected by the collocated dual vaporizer SP-AMS in laser-off mode (Sect. S1.1). The comparison of each species between the laser-only SP-AMS and the dual vaporizer SP-AMS, operated in laser-off mode, provides valuable insights into the percent of mass internally mixed with rBC. This comparison assumes that the mass of refractory organics, sulfate, nitrate, and chloride material internally mixed with BC is low. To estimate the non-refractory mass of each species present between 1–2.5 µm, we used the size distributions measured by the dual vaporizer SP-AMS. From this, it was found that 72 % of sulfate, 69 % of organic aerosol, and more than 90 % of nitrate were present in the PM_1 fraction. When accounting for the instrument's size range difference, approximately 19 % of submicron organic mass during this study is internally mixed with rBC. However, this fraction exhibited considerable temporal variation, as indicated by the moderate r^2 of 0.49 (Fig. 1f). Overall, both Org_{BC} and $Org_{NR\text{-}PM_{2.5}}$ show similar diurnal profiles (Fig. 1b). However, a slightly higher proportion of organic mass is mixed with rBC at night and during the morning hours, with the fraction decreasing in the afternoon. This pattern is consistent with vehicles and industrial sources emitting an internal mixture of rBC and organics, while SOA production tends to enhance the growth of BC-free aerosols due to their higher surface area fraction. Supporting this hypothesis, only 2.4 % of sulfate mass is mixed with rBC, despite a stronger correlation between $SO_{4,BC}$ and non-refractory SO_4 ($r^2 = 0.79$; Fig. 1g). As sulfate is primarily formed through secondary processes in the atmosphere, this limited presence of sulfate on soot particles indicates that the bulk of sulfate is externally mixed from rBC. Like SOA, the condensation of sulfate is likely to occur on all particles. However, the higher particle surface area of non-BC-containing aerosol will increase the fraction externally mixed from rBC. Furthermore, aerosol liquid water content is likely to be higher on parti-

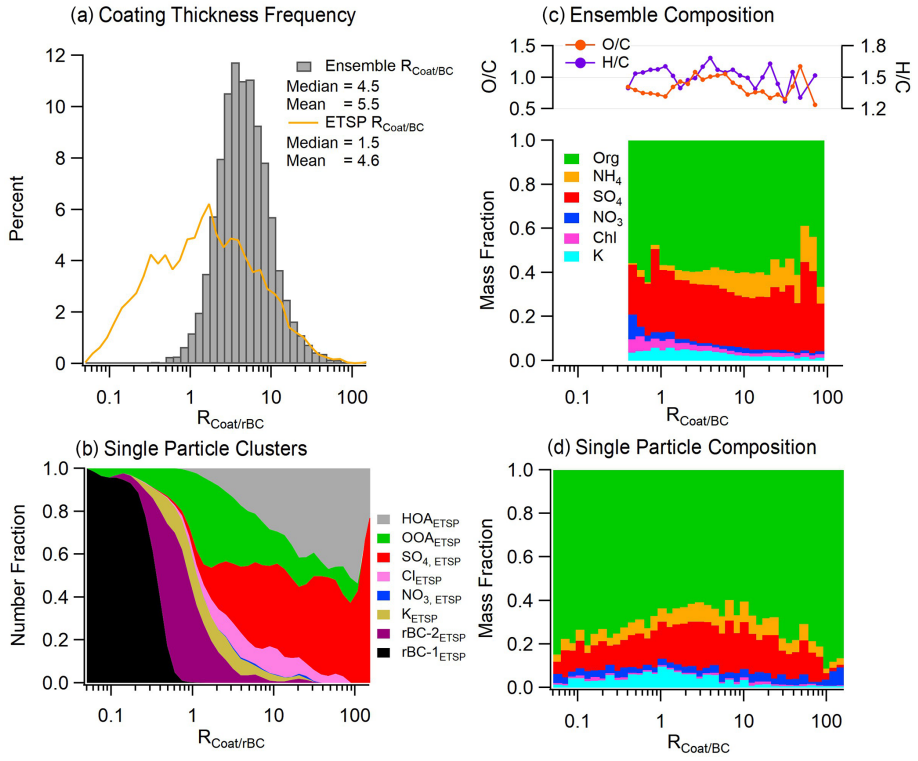

Figure 2. **(a)** Normalized frequency of $R_{\mathrm{coat\,/\,BC}}$ from the ensemble and ETSP measurements. **(b)** Frequency of each single-particle class as a function of $R_{\mathrm{coat\,/\,BC}}$. **(c)** Average mass fraction of ensemble measurements, divided by $R_{\mathrm{coat\,/\,BC}}$, and the O / C and H / C ratios of the organic coating. **(d)** Average mass fraction of single-particle measurements, divided by $R_{\mathrm{coat\,/\,BC}}$.

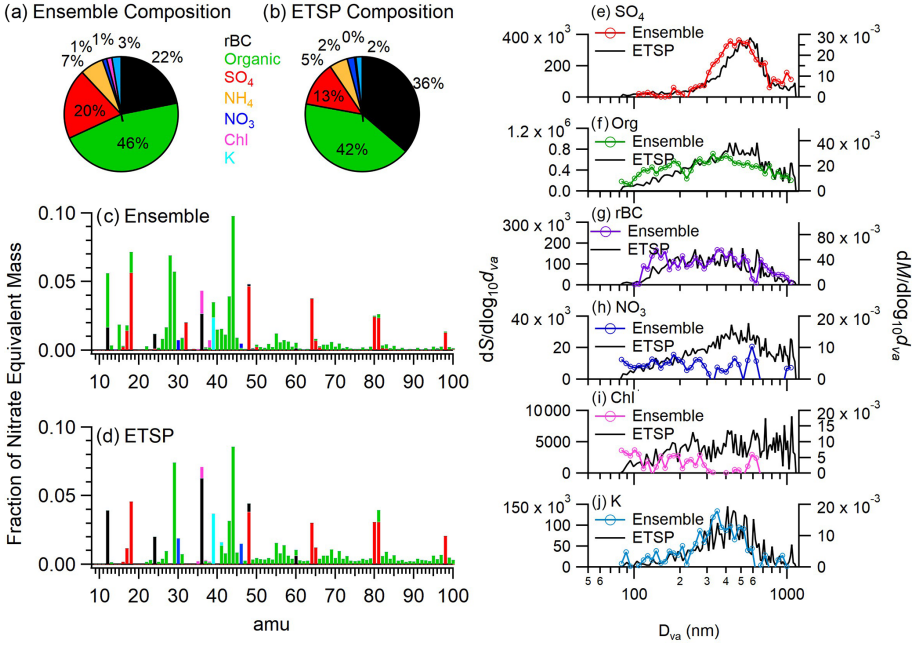

Figure 3. Average fractional composition of total $PM_{1,BC}$ measured by **(a)** high-resolution ensemble measurements and **(b)** ETSP measurements. **(c)** Average mass spectrum of ensemble measurements and **(d)** average mass spectrum of all single-particle events measured by ETSP mode. **(e–j)** Comparison of species-dependent size distributions for ensemble measurements (colored line) and ETSP measurements (black line). Bulk size distributions are mass weighted (against right y axes), while ETSP measurements are signal weighted (against left y axes).

cles free of rBC due to increased hygroscopicity, which promotes the aqueous phase formation of sulfate on non-BC-containing particles.

Nitrate, another secondary aerosol species, presents at low concentrations within both the rBC fraction and the NR-$PM_{2.5}$ fraction. High ambient temperatures throughout the measurement period likely promote the partitioning of inorganic nitrate into the gas phase. The negligible correlation between $NO_{3,BC}$ and $NO_{3,NR\text{-}PM_{2.5}}$, coupled with their different diurnal patterns (Fig. 1h), highlights the overall externally mixed nature of nitrate and soot aerosol and suggests different sources of nitrate between the two fractions. Additionally, differences in the aerosol water content or acidity between BC-containing and BC-free particles could also play a role in the weak correlation.

3.1.2 Single-particle characteristics of soot aerosol

Using the SP-AMS ETSP mode, we were able to further probe the single-particle composition and mixing state of BC-containing aerosol. Although the 14 699 single-particle spectra recorded only represent a small subset of ambient BC-containing aerosol, a comparison of the average composition, mass spectral features, and species-dependent size distributions measured during ETSP mode and ensemble mode indicates that the sampled single particles are generally representative of the soot population (Fig. 3). The mass fraction of rBC in $PM_{1,BC}$ was significantly higher in the single-particle measurements compared to the ensemble measurements, accounting for 36 % of $PM_{1,BC}$ in comparison to 22 % for the ensemble measurements. Concurrently, the $SO_{4,BC}$ mass fraction decreased from 20 % measured during ensemble mode to 13 % during ETSP mode. These differences could potentially arise from biases created by the specific m/z triggers selected for this study as has been observed previously (Lee et al., 2019). For example, one of the three triggers used was m/z 36 (C_3^+), which may introduce a bias towards events with high m/z 36 signal. Differences also appear when comparing the average mass spectra of all ensemble measurements (Fig. 3c) and all single-particle events (Fig. 3d), which likely arise due to variations between the HR and UMR fragmentation tables (Allan et al., 2004), in addition to the biases discussed above. Additionally, the average single-particle OA composition shows a slight enhancement of certain fragments, including m/z 60 and 73, two markers for biomass burning organic aerosol (BBOA; Cubison et al., 2011). This suggests there may a positive bias towards certain sources, such as BBOA.

Despite these differences, the species-dependent size distributions for $SO_{4,BC}$, Org_{BC}, rBC, and K_{BC} are similar between the bulk ensemble and ETSP measurements, suggesting that there is minimal systemic bias as a function of particle size (Fig. 3). However, the ETSP size distributions for $SO_{4,BC}$ and Org_{BC} are slightly shifted towards larger particle sizes. Additionally, the ensemble rBC size distribution shows an additional mode at small sizes. These differences may be attributed to larger particles generating more ions and thereby having a higher statistical likelihood of triggering an ETSP event.

Although rBC or other absorbing material is required for vaporization and subsequent detection with the laser-only SP-AMS configuration, 49 % of the ETSP spectra measured had no detectable rBC. The fraction of particles with no rBC was highest for the particle types with thickest coatings including hydrocarbon-like organic aerosol ($HOA_{BC,ETSP}$ (62 %)), $SO_{4,BC,ETSP}$ (45 %), and $OOA_{BC,ETSP}$ (35 %) particle clusters (Table S3). These seemingly rBC-free particles may represent events in which the particles did not overlap well with the laser vaporizer, resulting in temperatures that were sufficient to vaporize non-refractory coating material but not the rBC core (Onasch et al., 2012; Willis et al., 2014). Another possibility is that these particles were extremely thickly coated with only a small BC core, and the energy supplied by the laser vaporizer was only sufficient to vaporize the coating material, leaving the rBC intact. Finally, semi-volatile, BC-free particles may be thermally vaporized on heated internal surfaces, such as the ion filament, despite the absence of the tungsten vaporizer. This could be especially relevant for the $NO_{3,BC,ETSP}$ cluster due to the high volatility of ammonium nitrate. However, it is important to note that this cluster comprises only 247 particles, representing only 1.6 % of the total single particles detected (Fig. 5g). Particles without rBC signal were included for the clustering analysis but necessarily excluded from the calculation of $R_{coat\,/\,BC}$.

3.2 Sources and atmospheric processing of soot aerosol

3.2.1 Source apportionment using ensemble measurements

PMF analysis of the ensemble high-resolution mass spectra of soot particles resolved four distinct soot particle types characterized by distinct spectral features and tracer ions. These types include an oxidized organic aerosol ($OOA_{BC,PMF}$) factor, an oxidized rBC-rich factor (O-BC_{PMF}), a sulfate-rich factor ($SO_{4,BC,PMF}$), and a mixed biomass burning–mineral dust factor (BB-$K_{BC,PMF}$).

The $OOA_{BC,PMF}$ factor has an average concentration of $0.10 \pm 0.19\,\mu g\,m^{-3}$, constituting 29 % of the $PM_{1,BC}$ mass (Fig. 4). This soot type is primarily composed of organic species, which contribute 79 % of the mass, with the rest of the mass comprised of rBC (14 %), nitrate (4 %), and sulfate (3 %). The organic fraction is moderately oxidized with an O / C of 0.68 and shows enhanced levels of $C_2H_3O^+$ and CO_2^+, two markers for SOA (Ng et al., 2011). However, there is also an enhancement of $C_xH_y^+$ fragments, including $C_3H_3^+$ (m/z 39.02), $C_3H_5^+$ (m/z 41.04), $C_4H_7^+$ (m/z 55.05), and $C_4H_9^+$ (m/z 57.07), which are frequently used as markers

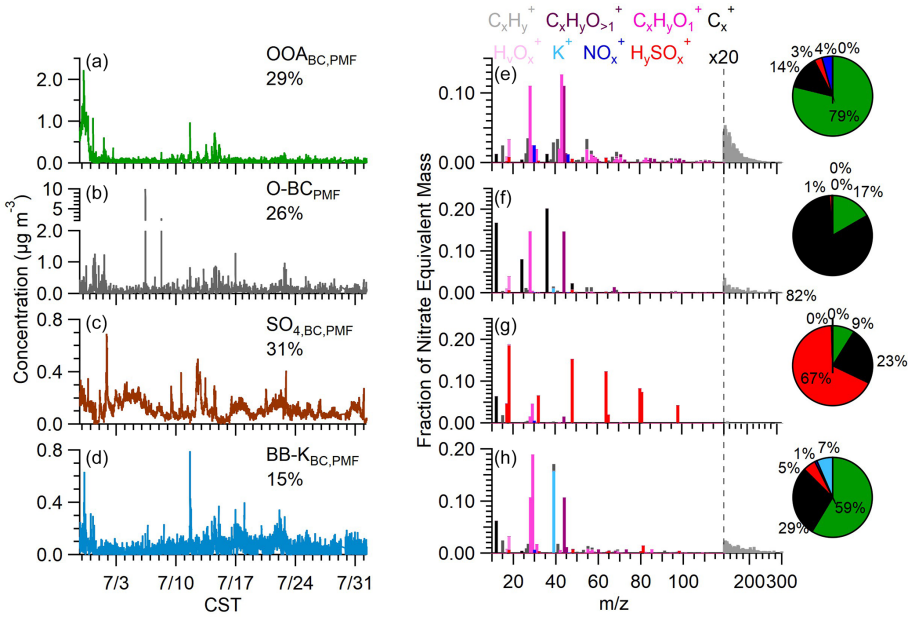

Figure 4. **(a–d)** Concentration time series of the PMF factors. Values reported are percent of total $PM_{1,BC}$. **(e–h)** Normalized, nitrate-equivalent mass spectra of PMF factors. Pie charts show the mass fraction of each species after the applying species-dependent relative ionization efficiency (RIE).

for hydrocarbon-like OA (HOA) (Al-Naiema et al., 2018; Ge et al., 2012b; Young et al., 2016). Based on this, we conclude that this factor likely represents processed soot aerosol with coatings containing a mixture of SOA and oxidized primary OA. Additionally, 80 % of the nitrate signal is attributed to this factor. The concentration of this factor peaks in the afternoon, consistent with secondary photochemical production (Fig. S7). However, there is also a minor increase corresponding with morning rush hour, emphasizing the contribution of primary aerosol (Fig. S7a). The time series shows the highest concentrations on 28–29 June, during which back trajectories are related to long-range transport from the continental United States (Fig. S8b).

The O-BC$_{PMF}$ spectrum is dominated by the C_{1-33}^+ peaks, with the rBC and organic fragments contributing 82 % and 17 % of the mass respectively. The most abundant organic fragment is CO_2^+, and the spectrum also shows an enhancement of the $C_3O_2^+$ ion (m/z 67.99). These ions serve as a marker for oxidized functional groups on the soot surface (Falk et al., 2021; Ma et al., 2023). Elevated $C_3O_2^+$ and CO_2^+ signals have also been identified in POA emitted from diesel and gasoline vehicles and in soot particles emitted from wood or fossil fuel combustion (Carbone et al., 2019; Collier et al., 2015; Corbin et al., 2014, 2015). There is also a slightly enhanced signal from reduced hydrocarbons such as $C_4H_7^+$ (m/z 55.05) and $C_4H_9^+$ (m/z 57.07), indicating that traffic emissions may be a source of this particle type. Indeed, the diurnal profile shows a clear increase at 07:00 LT and a minor increase at 16:00 LT, consistent with typical rush hours (Fig. S7b). Based on these temporal features, we conclude that this factor likely represents emissions from both gasoline light-duty vehicles and industrial or diesel vehicle sources. The average concentration of O-BC$_{PMF}$ was $0.102 \pm 0.193\ \mu g\ m^{-3}$; however, sporadic spikes were also seen, with concentrations occasionally reaching $10\ \mu g\ m^{-3}$. The most intense of these instances occurred on 7 July, coinciding with a plume observed near the site; however, the fuel type for this event is unknown (Fig. 4b).

The SO$_{4,BC,PMF}$ factor is dominated by $H_ySO_x^+$ ions, which contribute 67 % of the factor mass, along with relatively minor contribution from rBC (23 %) and organics (9 %). The time series shows a consistent background presence of this factor throughout the measurement period, with an average loading of $0.117 \pm 0.071\ \mu g\ m^{-3}$ (31 % of $PM_{1,BC;}$ Fig. 4c). The low organic content suggests that this factor is mainly comprised of inorganic sulfate that has condensed onto ambient rBC particles. Overall, SO$_{4,BC,PMF}$ accounts for over 90 % of the measured sulfate mass within soot aerosol. Rather than being associated with a specific source region, this factor appears to be a component of the regional background and is likely influenced by offshore sources (Fig. S8d).

An important source of non-sea salt sulfate in coastal regions is the oxidation of dimethyl sulfide (DMS), a byproduct from phytoplankton activity (Andreae, 1990; Andreae et al., 1985; Bates et al., 1992). Additionally, Bates et al. (2008) estimated that marine vessel emissions were the dominant source of sulfate over the Gulf of Mexico in 2006. However, recent regulations implemented in 2020 limit the sulfur content in marine heavy fuel oil to 0.1 % by mass within

the North American emissions control area (ECA) and 0.5 % in international waters (IMO, 2020). These policies have led to a noteworthy 80 % reduction in SO_x emissions and 72 % reduction in PM_1 emissions associated with shipping (Anastasopolos et al., 2021; Watson-Parris et al., 2022; Yu et al., 2020). Consequently, marine vessel emissions may contribute a smaller amount of sulfate and PM in this study compared to previous campaigns. Further discussion regarding the identification of shipping emissions is provided in Sect. 3.3.

The fourth factor, denoted as BB-$K_{BC,PMF}$, is notable for a significant contribution from K^+ and accounts for 95 % of the total K^+ mass observed within soot aerosol. The average loading of BB-$K_{BC,PMF}$ was $0.058 \pm 0.059\,\mu g\,m^{-3}$ with potassium contributing 7 % of the total mass. The remaining mass consists of organic (59 %), rBC (29 %), and sulfate (5 %). We propose that this factor represents a composite of biomass burning (BB) soot aerosol intermixed with mineral dust. Several key indicators support this hypothesis. K^+ is often used as a molecular marker for biomass combustion processes (Andreae, 1983), and the BB-$K_{BC,PMF}$ spectrum shows a slight increase in $C_2H_4O_2^+$ (m/z 60) and $C_3H_5O_2^+$ (m/z 73), which are markers for anhydrous sugars such as levoglucosan that are commonly emitted during BB processes (Cubison et al., 2011). However, the K^+ time series also shows multi-day events between 16 and 23 July which coincide with enhancements of coarse-mode aerosol volume ($V_{P,1-10\,\mu m}$) and aerosol light absorption. These events are likely related to Saharan mineral dust transported from West Africa (Fig. S9a; Gorkowski et al., 2024). The presence of Saharan dust in the Houston area has been well documented (Bates et al., 2008; Bozlaker et al., 2013, 2019; Das et al., 2022), and the HYSPLIT concentration-weighted back trajectories for this period indicate an obvious source region close to West Africa (Fig. S8e). Fe^+, another major component in Saharan dust, shows sporadic enhancements throughout the campaign, and these occurrences often, but not always, coincide with elevated concentrations of K^+ (Fig. S9). Likewise, Na^+ was also intermittently detected. However, this element appears to be related to biomass burning aerosol as highlighted by the simultaneous increases of Na^+ and $C_2H_4O_2^+$ (Fig. S9). While Na^+ has previously been identified in BB aerosol (Jahn et al., 2021), not all periods with elevated $C_2H_4O_2^+$ coincide with Na^+ increases. This suggests that only certain fuel types or combustion conditions emit Na^+. Previous SP-AMSs have linked Na^+ with vehicle emissions (Rivellini et al., 2020). However, we observe low correlations ($r^2 < 0.1$) between Na^+ and HOA marker ions such as $C_4H_7^+$ and $C_4H_9^+$.

3.2.2 Origins of soot particle according to single-particle measurements

Eight distinct BC particle types were identified by applying K-means clustering to the ETSP measurements (Fig. 5). These include a hydrocarbon-like OA ($HOA_{BC,ETSP}$), two rBC-rich classes displaying different amounts of BC content (rBC-1_{ETSP} and rBC-2_{ETSP}), an oxidized OA classes ($OOA_{BC,ETSP}$), a sulfate-rich class ($SO_{4,BC,ETSP}$), a chloride-rich class ($Cl_{BC,ETSP}$), a nitrate-rich class ($NO_{3,BC,ETSP}$), and a potassium-rich class ($K_{BC,ETSP}$).

$HOA_{BC,ETSP}$ is the most abundant particle type by number, with 3851 particle counts (26 %). The average spectrum displays characteristic hydrocarbon peaks at m/z 41, 43, 55, 57, 69, and 71, consistent with previous measurements of vehicle exhaust (Fig. 5a) (Canagaratna et al., 2004; Collier et al., 2015). The elevated m/z 44 signal indicates the aerosol has undergone some degree of processing (Willis et al., 2016; Zhang et al., 2005). The diurnal profile shows two increases at 06:00–08:00 and 15:00–16:00 LT, corresponding with morning and afternoon rush hours, respectively (Fig. S7e). C_x^+ peaks only account for 5 % of the average total mass within this aerosol type, indicating substantial coating mass. Additionally, The $HOA_{BC,ETSP}$ class shows a broad mass-based size distribution between 200–1000 nm in D_{va}. This is in contrast to other AMS measurements, which often identify HOA with size distributions in sizes less than 150 nm (Collier et al., 2015; Lee et al., 2019; Ulbrich et al., 2012; Zhang et al., 2005). The larger particle size and small mass fraction of rBC observed here suggest that the particles grouped in the $HOA_{BC,ETSP}$ class are a result of the rapid condensation of lubricating oil and other low-volatility vapors onto BC cores or the coagulation of BC-free HOA-like particles with BC-containing particles within the vehicle exhaust system. While previous studies have detected lubricating oil signatures in vehicle POA (Collier et al., 2015; Sonntag et al., 2012; Worton et al., 2014), these results provide direct evidence that the smaller particles identified in these previous studies may be externally mixed from rBC. Another possibility is that smaller HOA particles generate fewer ions and are less likely to trigger an event as discussed in Sect. 3.1.2. These particles may also originate from other fossil fuel combustion sources, such as emissions from heavy fuel oil used in ship traffic. Direct measurements of ultra-low sulfur diesel fuel emissions, similar to what ships use near shore and in US ports, show spectra similar to vehicle emissions (Price et al., 2017).

Two particle classes, rBC-1_{ETSP} and rBC-2_{ETSP}, were identified, each accounting for 9 % and 10 % of the particle number, respectively. Both classes are dominated by C_x^+ fragments, but the amount of coating material differs. The soot particles in the rBC-1_{ETSP} class are nearly uncoated, with nearly all particles having $R_{coat\,/\,BC}$ less than 1. In contrast to this, those in the rBC-2_{ETSP} class have higher contributions from organics, sulfate, and potassium with rBC accounting for 49 % of mass on average. Both rBC-1_{ETSP} and rBC-2_{ETSP} show increased concentrations in the afternoon, concurrent with the increases in HOA_{ETSP}, OOA_{PMF}, and O-BC_{PMF}. However, unlike these other particle types, little enhancement of rBC-1_{ETSP} and rBC-2_{ETSP} is seen during

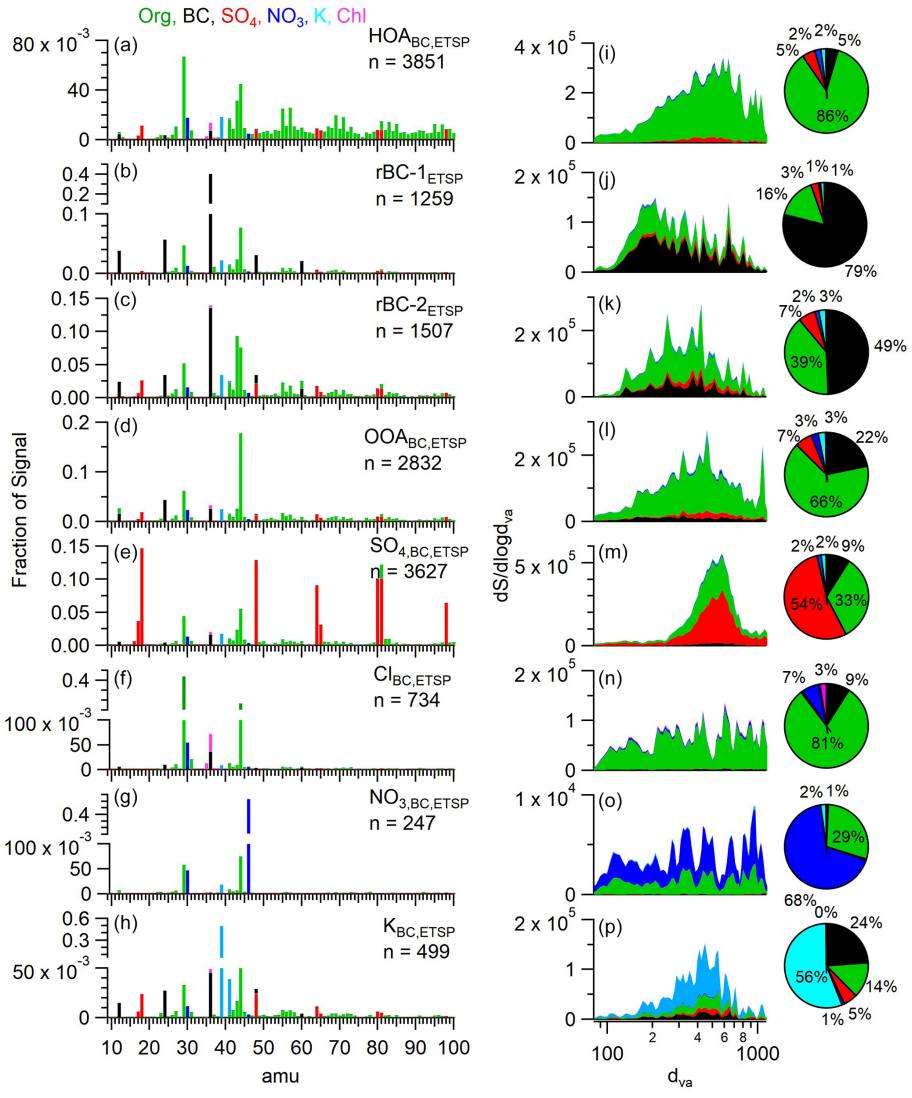

Figure 5. **(a–h)** Average mass spectra of each ETSP cluster calculated using K-means clustering. Number of particles in each class is also displayed. **(i–p)** Signal-weighted size distribution of each cluster. Pie charts display the mass fraction of each aerosol species.

morning rush hour. This suggests the presence of local, non-vehicle rBC sources or meteorological conditions conducive to the transport of fresh emissions to the sampling site during the afternoon and are likely related to industrial emissions or gas flaring. Direct measurements of PM emissions from gas-flaring activity observed extremely thinly coated soot particles with BC mass fraction between 80 %–96 % (Fortner et al., 2012). The presence of sulfate (7 %) and potassium (3 %) in rBC-2_{ETSP} may indicate co-emission from refineries or biomass burning, respectively. The organic signal at m/z 60 appears to be elevated, further supporting the influence of BB. However, the attribution of m/z 60 between C_5^+ and organic fragments in the ETSP analysis is uncertain. Additionally, the size distribution shifted from a peak at 200 nm for rBC-1_{ETSP} to 400 nm for rBC-2_{ETSP}, consistent with the condensation of secondary material.

The average spectrum of the $OOA_{BC,ETSP}$ particle cluster was dominated by m/z 44, suggesting significant oxidation of the organic material. Indeed, the fraction of mass at m/z 44 (f_{44}) for $OOA_{BC,ETSP}$ is higher than that of $OOA_{BC,PMF}$, indicating that particles within this cluster are more oxidized than the PMF factor. The diurnal profile of this class is relatively flat with only a modest increase in the afternoon, suggesting that $OOA_{BC,ETSP}$ represents regionally transported background aerosols that have undergone photochemical processing.

Similar to the $SO_{4,BC,PMF}$ factor, soot particles in the $SO_{4,BC,ETSP}$ class show a large contribution from H_ySO_x fragments, with sulfate accounting for 54 % of the total mass on average. The majority of the rest of the material is composed of organic species (33 %) and rBC (9 %). These particles likely represent the incorporation of inorganic sul-

fate and other secondary organic material with rBC particles through processes such as condensation or coagulation. Given that most of the sulfate signal was attributed to this particle class, this indicates that particulate sulfate, which is primarily formed through the secondary oxidation of $SO_{2(g)}$, is generally externally mixed from organic aerosol. This class shows the largest size mode, peaking at 600 nm. As sulfate is efficiently produced in the aqueous phase, this contribution of mass in the droplet mode is consistent with aqueous phase production. $SO_{4,BC,ETSP}$ consisted of thickly coated particles, with a median coating thickness of 9.5 (Fig. 2b).

The average spectrum of soot particles within the $Cl_{BC,ETSP}$ cluster is primarily composed of m/z 29 and 44. However, it is notable as the only particle class with measurable chloride, which accounts for 2.5 % of the mass. The average cluster mass spectrum shows minor enhancements of m/z 60 and 73, suggesting a potential association with oxidized BB aerosol. Particles of this type were relatively infrequent, only accounting for 5 % of the measured particles.

The $K_{BC,ETSP}$ shows the highest contribution of K^+, accounting for 56 % of the average particle mass in this cluster. The average spectrum shows minor contribution from m/z 36 (C_3^+) and m/z 44 (CO_2^+). This is in contrast to $K_{BC,PMF}$, which shows a significantly higher contribution from oxidized organic fragments. Recent single-particle measurements of ambient biomass burning emissions revealed that some types of BBOA particles are relatively enriched with K^+ compared with other BBOA particle types (Lee et al., 2016). Furthermore, a near-roadside study in Fontana identified a similar K^+-dominated particle cluster that the authors attributed to vehicle emissions (Lee et al., 2019). However, the Fontana K class displayed a smaller average diameter and more signal at m/z 43 and 55 than the $K_{BC,ETSP}$ cluster identified in this work. The low contribution of markers for primary HOA (i.e., m/z 55, 57) and BBOA (i.e., m/z 60, 73), in conjunction with the presence of secondary material such as sulfate, suggests that particles of this type have undergone atmospheric processing. From this, we conclude that the $K_{BC,ETSP}$ class represents a subset of relatively aged potassium-containing particles from sources such as vehicles, biomass burning, and/or mineral dust. This class only consisted of 499 particles (3.4 % of total) with a size distribution peaking at 400–600 nm.

Finally, the nitrate class was the least abundant with only 247 particles (1.5 %). The average spectrum is dominated by m/z 46 (NO_2^+) with only a small enhancement of m/z 30 (NO^+) and m/z 44. Overall, nitrate accounted for an average of 68 % of particle mass in this cluster. The extremely low contribution from rBC is consistent with the overall external mixing state of nitrate and rBC as discussed previously.

3.3 Sources of refractory metal compounds in soot aerosol

An advantage of the laser vaporization utilized in the SP-AMS is the ability to detect refractory metal compounds internally mixed with rBC (Bibi et al., 2021; Cao et al., 2022; Carbone et al., 2015; Rivellini et al., 2020). Heavy fuel oil combustion from shipping activity is typically associated with the emission of heavy metals, such as vanadium (V) and nickel (Ni) (Popovicheva et al., 2012; Rivellini et al., 2020). Indeed, a previous study concluded that shipping activities are the primary source of V-rich aerosol in the Houston region (Bozlaker et al., 2019). Two events with elevated V^+ concentration are detailed in Fig. S10. These events coincided with increases in particulate sulfate and rBC, supporting the role of shipping-related emissions. However, there is negligible correlation ($r^2 < 0.05$) between V^+ and sulfate for the entire campaign, indicating that primary ship emissions are not the major source of sulfate for most of this campaign.

Finally, there is a noticeable increase in K^+ and Fe^+ levels on the night of 4 July, which we attribute to firework activity. A previous SP-AMS study found enhancement of various metal species, including these ions, when fireworks were used (Bibi et al., 2021). However, the primary firework tracer identified in Bibi et al. (2021) was Sr^+, which was absent in our data. The lack of Sr^+ may be due to significantly lower concentrations during this campaign or the utilization of different types of fireworks.

3.4 Black carbon mixing state

Figure 6a presents the distribution of single-particle diversity (D_i) for each of the particle classes. D_i is a measurement of the effective number of species present in individual species and ranges from 1 to 6 in this work. Particles in the $HOA_{BC,ETSP}$ (average $D_i = 1.5$) and $OOA_{BC,ETSP}$ (average $D_i = 1.9$) classes show low D_i values as the composition is dominated by organic aerosol. Likewise, particles in the rBC-1_{ETSP} class also show low D_i as they have a high mass fraction of rBC. In contrast, rBC-2_{ETSP} (average $D_i = 2.3$), $SO_{4,ETSP}$ (2.2), and K_{ETSP} (2.7) display the highest diversity. All three of these classes likely consist of particles that have undergone atmospheric processing with significant contribution from secondary material such as organics and sulfate as well as primary species such as rBC and K. This highlights the role of photochemical processing in modulating the aerosol mixing state.

The mixing state index (χ) indicates the degree of aerosol heterogeneity and ranges between 0 % (fully externally mixed) and 100 % (fully internally mixed). In this study, the hourly averages of χ range from 5 % to 95 %, with an average of 41 ± 13 % (Fig. 7a). The bulk aerosol diversity (D_γ) calculated from the ensemble measurements exhibits a daytime decrease, indicating reduced aerosol population diversity during the day (Fig. S7n). This decrease corresponds to

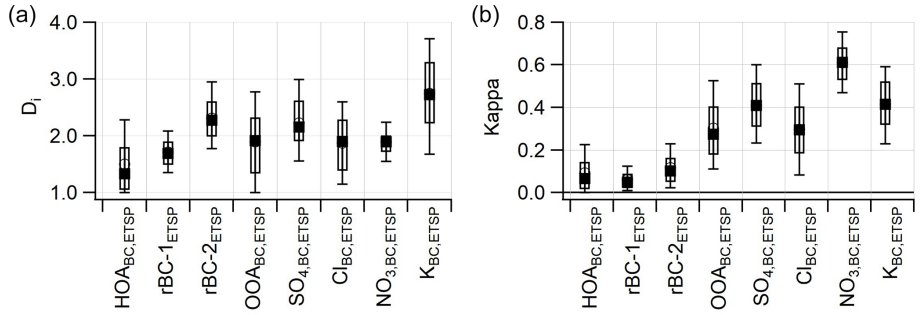

Figure 6. **(a)** Single-particle diversity (D_i) for each cluster type. **(b)** Predicted hygroscopicity for individual particles, divided by particle class. The solid and open markers indicate the median and mean respectively. The box indicates the 25th–75th percentile, and whiskers indicate 10th–90th percentiles.

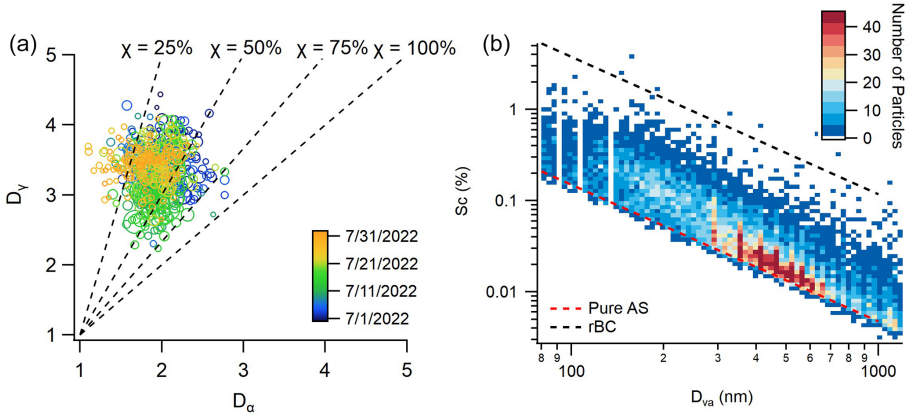

Figure 7. **(a)** Mixing state diagram depicting the relationship between bulk particle diversity (D_γ) and average single-particle diversity (D_α). The dashed lines indicate the resulting mixing state index (χ). Points are sized by $PM_{1,rBC}$ concentration and colored by sampling date. **(b)** Bivariate histogram of estimated particle critical supersaturation and particle diameter. Dashed lines represent uncoated rBC ($\kappa = 0.001$) and pure ammonium sulfate ($\kappa = 0.61$).

elevated mass fractions of organics and sulfate. In contrast to this, the single-particle diversity (D_α) shows little diurnal variation, with only a slight decrease in the afternoon. As a result, there is an overall daytime increase in the mixing state index (χ). Our results indicate that the production of SOA and sulfate coatings on rBC through photochemical processes results in a more internally mixed, homogenous aerosol population. Finally, at night, sulfate concentration remains elevated, while organic and rBC decrease, resulting in an increase in D_γ but a decrease in the mixing state index. In contrast to these results, Lee et al. (2019) reported elevated values for both D_α and D_γ during rush hour in Fontana, CA, where the rapid secondary formation of particulate nitrate played a key role in rBC mixing state. The observed differences can be explained by the complex combination of rBC sources in Houston and differences in aerosol acidity.

3.5 Effect of mixing state on particle hygroscopicity

The ability for a particle to act as a CCN is governed by its bulk hygroscopicity. Previous studies have used measurements of single-particle composition to quantitatively predict their hygroscopicity. These estimates have been found to agree well with direct measurements of water uptake using instruments such as a hygroscopic tandem differential mobility analyzer (HTDMA) (Gysel et al., 2007; Healy et al., 2014; Petters and Kreidenweis, 2007; X. Wang et al., 2020). Figure 6b shows the predicted hygroscopicity parameter κ for the BC-containing particles measured in this study grouped by particle classes. Details about the calculation of κ, estimation of single-particle O / C and H / C values, and the necessary assumptions are provided in Sect. S1.4 and S1.5.

Among the eight particle classes, the $HOA_{BC,ETSP}$ and $rBC\text{-}1_{ETSP}$ classes show the lowest hygroscopicity, with average κ of 0.09 and 0.06, respectively. Although most particles in the $HOA_{BC,ETSP}$ class have a low rBC volume fraction, the organic species present are chemically reduced and display extremely low κ_{org} values, resulting in a decrease in overall particle hygroscopicity (Fig. S11). This is consistent with direct measurements of motor oil and diesel emissions, which show little hygroscopic growth (Fofie et al.,

2018; Lambe et al., 2011). Despite the presence of relatively hygroscopic coating material on rBC-1_{ETSP} and rBC-2_{ETSP}, the high rBC volume fraction results in extremely low overall κ for both classes. However, the rBC-2_{ETSP} class shows slightly higher κ values than rBC-1_{ETSP} due to a higher fraction of oxidized organic material and inorganic sulfate.

The median predicted κ for $OOA_{BC,ETSP}$ of 0.27 agrees well with SOA produced in laboratory and chamber experiments, as well as OOA measured in other field studies (Chang et al., 2010; Fofie et al., 2018). Additionally, due to the high mass fraction of sulfate in $SO_{4,BC,ETSP}$ particles, the κ value approaches that of pure ammonium sulfate (0.61) for a subpopulation of this particle type. Similarly, the κ values for $NO_{3,BC,ETSP}$ and $K_{BC,ETSP}$ approach that of ammonium nitrate (0.67) and potassium sulfate (0.69), respectively. As these inorganic salts are hygroscopic, the overall hygroscopicity of these particles is highest. The presence of rBC particles internally mixed with hygroscopic material is consistent with the rapid aging of BC aerosol previously observed in Houston (Peng et al., 2016; Wang et al., 2018). Understanding the formation of hydrophilic coating material on rBC particles is necessary for accurate representations of global BC burden and can aid in resolving model biases observed in the Arctic (Liu et al., 2016; Wang et al., 2018).

4 Conclusions

This study involved the measurements of both the bulk and single-particle composition of soot particles using a SP-AMS operated in the laser-only configuration. Material internally mixed with BC had a significant contribution from secondary aerosol species, including oxidized organic aerosol and inorganic sulfate. This finding highlights the importance of atmospheric aging processes affecting soot aerosol characteristics in urban environments. The utilization of two different source apportionment techniques in this study, namely PMF of the ensemble measurements and K-means clustering of the single-particle measurements, yields complementary results. Although PMF analysis of the ensemble spectra failed to isolate a factor related to HOA, either due to low signal intensity or a similar temporal profile as other OA sources, the simultaneous application of the ETSP mode successfully identified particles exhibiting HOA-like spectra. Additionally, both source apportionment techniques revealed the presence of nearly pure rBC particles with extremely small amounts of coating material. For instance, the average $R_{coat\,/\,BC}$ for the oxidized rBC factor (O-BC_{PMF}) was only 0.24, while the median value for the rBC-1_{ETSP} single-particle cluster was 0.20.

A significant limitation in the ETSP data interpretation is the reliance on UMR mass spectra due to the extremely low ion counts for individual particle events. This introduces uncertainty when distinguishing different aerosol species that share isobaric ions, such as C_4^+ and SO^+ or C_5^+ and $C_2H_4O_2^+$. Additionally, the lack of high-resolution spectra hinders the differentiation of isobaric ions representing distinct organic ion families, such as $C_4H_7^+$ and $C_3H_3O^+$ at m/z 55, which would otherwise contribute to more robust differentiation between POA and SOA factors, such as HOA and OOA.

The utilization of single-particle measurements also allowed for a detailed analysis of the BC mixing state. The average mixing state index (χ) was determined to be 41 ± 13 %, indicating that the aerosol population demonstrated an intermediate between internal and external mixing. Notably, these values align with the χ values measured at two other cities, including a near-roadside location in Fontana, CA (48 %), and a downtown location in Pittsburgh, PA (43 %) (Lee et al., 2019; Ye et al., 2018). κ-Köhler theory was utilized to estimate critical supersaturation values at which these particles would activate into cloud droplets (Fig. 7b). Many of the BC-containing particles had undergone atmospheric processing and exhibited mixing with hygroscopic material. Consequently, a significant fraction of the soot particles demonstrates sufficiently high κ values and diameters to activate under atmospherically relevant supersaturation values. Among the classes identified, the $OOA_{BC,ETSP}$ and $SO_{4,BC,ETSP}$ type particles appear to be particularly relevant for CCN activity, given their combined attributes of abundance, hygroscopicity, and size distribution. This finding has important implications for understanding the activation of rBC containing particles into cloud droplets and the sources of CCN in urban locations.

Code availability. The SQUIRREL and PIKA toolkits are available at https://cires1.colorado.edu/jimenez-group/ToFAMSResources/ToFSoftware/index.html (University of Colorado, 2024). HYSPLIT is available at https://www.ready.noaa.gov/HYSPLIT.php (NOAA, 2024).

Data availability. All data for TRACER are available online from the Atmospheric Radiation Measurement (ARM) at https://doi.org/10.5439/1958716 (Farley and Zhang, 2023).

Supplement. The supplement related to this article is available online at: https://doi.org/10.5194/acp-24-3953-2024-supplement.

Author contributions. QZ and RNF conceptualized the research aims. QZ, CDC, ACA, and MKD planned the field campaign. RNF, LHR, AKYL, and QZ carried out the SP-AMS measurements and data analyses. JEL, RDL, CDC, KG, ASMS, KBB, ACA, and MKD provided supporting measurement data. RNF and QZ prepared the manuscript with input from all co-authors.

Competing interests. At least one of the (co-)authors is a member of the editorial board of *Atmospheric Chemistry and Physics*.

The peer-review process was guided by an independent editor, and the authors also have no other competing interests to declare.

Disclaimer. Publisher's note: Copernicus Publications remains neutral with regard to jurisdictional claims made in the text, published maps, institutional affiliations, or any other geographical representation in this paper. While Copernicus Publications makes every effort to include appropriate place names, the final responsibility lies with the authors.

Acknowledgements. This research was supported by the U.S. Department of Energy's Atmospheric System Research Program (grant nos. DE-SC0021242, DE-SC0022140, and LANL KP1701010) and the California Agricultural Experiment Station (project CA-D-ETX-2102-H). Ryan N. Farley also acknowledges funding from the Jastro-Shields Research Award and the Donald G. Crosby Fellowship in Environmental Chemistry from the University of California at Davis.

Financial support. This research has been supported by the U.S. Department of Energy (grant nos. DE-SC0021242, DE-SC0022140, and LANL KP1701010), the California Agricultural Experiment Station (project CA-D-ETX-2102-H), the Jastro-Shields Research Award, and the Donald G. Crosby Fellowship in Environmental Chemistry from the University of California at Davis.

Review statement. This paper was edited by Stefania Gilardoni and reviewed by two anonymous referees.

References

Ahmed, M., Rappenglück, B., Das, S., and Chellam, S.: Source apportionment of volatile organic compounds, CO, SO_2 and trace metals in a complex urban atmosphere, Environ. Adv., 6, 100127, https://doi.org/10.1016/j.envadv.2021.100127, 2021.

Allan, J. D., Delia, A. E., Coe, H., Bower, K. N., Alfarra, M. R., Jimenez, J. L., Middlebrook, A. M., Drewnick, F., Onasch, T. B., Canagaratna, M. R., Jayne, J. T., and Worsnop, D. R.: A generalised method for the extraction of chemically resolved mass spectra from Aerodyne aerosol mass spectrometer data, J. Aerosol Sci., 35, 909–922, https://doi.org/10.1016/j.jaerosci.2004.02.007, 2004.

Al-Naiema, I. M., Hettiyadura, A. P. S., Wallace, H. W., Sanchez, N. P., Madler, C. J., Cevik, B. K., Bui, A. A. T., Kettler, J., Griffin, R. J., and Stone, E. A.: Source apportionment of fine particulate matter in Houston, Texas: insights to secondary organic aerosols, Atmos. Chem. Phys., 18, 15601–15622, https://doi.org/10.5194/acp-18-15601-2018, 2018.

Anastasopolos, A. T., Sofowote, U. M., Hopke, P. K., Rouleau, M., Shin, T., Dheri, A., Peng, H., Kulka, R., Gibson, M. D., Farah, P., and Sundar, N.: Air quality in Canadian port cities after regulation of low-sulphur marine fuel in the North American Emissions Control Area, Sci. Total Environ., 791, 147949, https://doi.org/10.1016/j.scitotenv.2021.147949, 2021.

Andreae, M. O.: Soot carbon and excess fine potassium: Long-range transport of combustion-derived aerosols, Science, 220, 1148–1151, https://doi.org/10.1126/science.220.4602.1148, 1983.

Andreae, M. O.: Ocean-atmosphere interactions in the global biogeochemical sulfur cycle, Mar. Chem., 30, 1–29, https://doi.org/10.1016/0304-4203(90)90059-L, 1990.

Andreae, M. O., Ferek, R. J., Bermond, F., Byrd, K. P., Engstrom, R. T., Hardin, S., Houmere, P. D., Lemarrec, F., and Raemdonck, H.: Dimethyl sulfide in the Marine atmosphere, J. Geophys. Res., 100, 12891–12900, https://doi.org/10.1029/95jd02374, 1985.

Avery, A. M., Williams, L. R., Fortner, E. C., Robinson, W. A., and Onasch, T. B.: Particle detection using the dual-vaporizer configuration of the soot particle Aerosol Mass Spectrometer (SP-AMS), Aerosol Sci. Tech., 55, 254–267, https://doi.org/10.1080/02786826.2020.1844132, 2020.

Banta, R. M., Senff, C. J., Nielsen-Gammon, J., Darby, L. S., Ryerson, T. B., Alvarez, R. J., Sandberg, S. R., Williams, E. J., and Trainer, M.: A bad air day in Houston, B. Am. Meteorol. Soc., 86, 657–669, https://doi.org/10.1175/BAMS-86-5-657, 2005.

Bates, T. S., Lamb, B. K., Guenther, A., Dignon, J., and Stoiber, R. E.: Sulfur emissions to the atmosphere from natural sourees, J. Atmos. Chem., 14, 315–337, https://doi.org/10.1007/BF00115242, 1992.

Bates, T. S., Quinn, P. K., Coffman, D., Schulz, K., Covert, D. S., Johnson, J. E., Williams, E. J., Lerner, B. M., Angevine, W. M., Tucker, S. C., Brewer, W. A., and Stohl, A.: Boundary layer aerosol chemistry during TexAQS/GoMACCS 2006: Insights into aerosol sources and transformation processes, J. Geophys. Res., 113, 1–18, https://doi.org/10.1029/2008JD010023, 2008.

Bean, J. K., Faxon, C. B., Leong, Y. J., Wallace, H. W., Cevik, B. K., Ortiz, S., Canagaratna, M. R., Usenko, S., Sheesley, R. J., Griffin, R. J., and Ruiz, L. H.: Composition and sources of particulate matter measured near Houston, TX: Anthropogenic-biogenic interactions, Atmosphere, 7, 73, https://doi.org/10.3390/atmos7050073, 2016.

Bibi, Z., Coe, H., Brooks, J., Williams, P. I., Reyes-Villegas, E., Priestley, M., Percival, C. J., and Allan, J. D.: Technical note: A new approach to discriminate different black carbon sources by utilising fullerene and metals in positive matrix factorisation analysis of high-resolution soot particle aerosol mass spectrometer data, Atmos. Chem. Phys., 21, 10763–10777, https://doi.org/10.5194/acp-21-10763-2021, 2021.

Bond, T. C. and Bergstrom, R. W.: Light absorption by carbonaceous particles: An investigative review, Aerosol Sci. Tech., 40, 27–67, https://doi.org/10.1080/02786820500421521, 2006.

Bond, T. C., Doherty, S. J., Fahey, D. W., Forster, P. M., Berntsen, T., Deangelo, B. J., Flanner, M. G., Ghan, S., Kärcher, B., Koch, D., Kinne, S., Kondo, Y., Quinn, P. K., Sarofim, M. C., Schultz, M. G., Schulz, M., Venkataraman, C., Zhang, H., Zhang, S., Bellouin, N., Guttikunda, S. K., Hopke, P. K., Jacobson, M. Z., Kaiser, J. W., Klimont, Z., Lohmann, U., Schwarz, J. P., Shindell, D., Storelvmo, T., Warren, S. G., and Zender, C. S.: Bounding the role of black carbon in the climate system: A scientific assessment, J. Geophys. Res.-Atmos., 118, 5380–5552, https://doi.org/10.1002/jgrd.50171, 2013.

Bozlaker, A., Prospero, J. M., Fraser, M. P., and Chellam, S.: Quantifying the contribution of long-range saharan dust transport on particulate matter concentrations in Houston, Texas, using de-

tailed elemental analysis, Environ. Sci. Technol., 47, 10179–10187, https://doi.org/10.1021/es4015663, 2013.

Bozlaker, A., Prospero, J. M., Price, J., and Chellam, S.: Identifying and Quantifying the Impacts of Advected North African Dust on the Concentration and Composition of Airborne Fine Particulate Matter in Houston and Galveston, Texas, J. Geophys. Res.-Atmos., 124, 12282–12300, https://doi.org/10.1029/2019JD030792, 2019.

Caicedo, V., Rappenglueck, B., Cuchiara, G., Flynn, J., Ferrare, R., Scarino, A. J., Berkoff, T., Senff, C., Langford, A., and Lefer, B.: Bay Breeze and Sea Breeze Circulation Impacts on the Planetary Boundary Layer and Air Quality From an Observed and Modeled DISCOVER-AQ Texas Case Study, J. Geophys. Res.-Atmos., 124, 7359–7378, https://doi.org/10.1029/2019JD030523, 2019.

Canagaratna, M. R., Jayne, J. T., Ghertner, D. A., Herndon, S., Shi, Q., Jimenez, J. L., Silva, P. J., Williams, P., Lanni, T., Drewnick, F., Demerjian, K. L., Kolb, C. E., and Worsnop, D. R.: Chase studies of particulate emissions from in-use New York City vehicles, Aerosol Sci. Tech., 38, 555–573, https://doi.org/10.1080/02786820490465504, 2004.

Cao, L. M., Wei, J., He, L. Y., Zeng, H., Li, M. L., Zhu, Q., Yu, G. H., and Huang, X. F.: Aqueous aging of secondary organic aerosol coating onto black carbon: Insights from simultaneous L-ToF-AMS and SP-AMS measurements at an urban site in southern China, J. Clean. Prod., 330, 129888, https://doi.org/10.1016/j.jclepro.2021.129888, 2022.

Cappa, C. D., Onasch, T. B., Massoli, P., Worsnop, D. R., Bates, T. S., Cross, E. S., Davidovits, P., Hakala, J., Hayden, K. L., Jobson, B. T., Kolesar, K. R., Lack, D. A., Lerner, B. M., Li, S., Mellon, D., Nuamaan, I., Olfert, J. S., Petaja, T., Quinn, P. K., Song, C., Subramanian, R., Williams, E., and Zaveri, R. A.: Radiative Absorption Enhancements Due to the Mixing State of Atmospheric Black Carbon, Science, 337, 1078–1082, https://doi.org/10.1126/science.1223447, 2012.

Cappa, C. D., Zhang, X., Russell, L. M., Collier, S., Lee, A. K. Y., Chen, C. L., Betha, R., Chen, S., Liu, J., Price, D. J., Sanchez, K. J., McMeeking, G. R., Williams, L. R., Onasch, T. B., Worsnop, D. R., Abbatt, J., and Zhang, Q.: Light Absorption by Ambient Black and Brown Carbon and its Dependence on Black Carbon Coating State for Two California, USA, Cities in Winter and Summer, J. Geophys. Res.-Atmos., 124, 1550–1577, https://doi.org/10.1029/2018JD029501, 2019.

Carbone, S., Onasch, T., Saarikoski, S., Timonen, H., Saarnio, K., Sueper, D., Rönkkö, T., Pirjola, L., Häyrinen, A., Worsnop, D., and Hillamo, R.: Characterization of trace metals on soot aerosol particles with the SP-AMS: detection and quantification, Atmos. Meas. Tech., 8, 4803–4815, https://doi.org/10.5194/amt-8-4803-2015, 2015.

Carbone, S., Timonen, H. J., Rostedt, A., Happonen, M., Keskinen, J., Ristimaki, J., Korpi, H., Artaxo, P., Worsnop, D., Canonaco, F., Prévôt, A. S. H., Hillamo, R., Saarikoski, S., Keskinen, J., Ristimaki, J., Korpi, H., Artaxo, P., Canagaratna, M., Worsnop, D., Canonaco, F., Prévôt, A. S. H., Hillamo, R., and Saarikoski, S.: Distinguishing fuel and lubricating oil combustion products in diesel engine exhaust particles, Aerosol Sci. Tech., 53, 594–607, https://doi.org/10.1080/02786826.2019.1584389, 2019.

Chang, R. Y.-W., Slowik, J. G., Shantz, N. C., Vlasenko, A., Liggio, J., Sjostedt, S. J., Leaitch, W. R., and Abbatt, J. P. D.: The hygroscopicity parameter (κ) of ambient organic aerosol at a field site subject to biogenic and anthropogenic influences: relationship to degree of aerosol oxidation, Atmos. Chem. Phys., 10, 5047–5064, https://doi.org/10.5194/acp-10-5047-2010, 2010.

Collier, S., Zhou, S., Kuwayama, T., Forestieri, S., Brady, J., Zhang, M., Kleeman, M., Cappa, C., Bertram, T., and Zhang, Q.: Organic PM emissions from vehicles: Composition, O / C ratio, and dependence on PM concentration, Aerosol Sci. Tech., 49, 86–97, https://doi.org/10.1080/02786826.2014.1003364, 2015.

Collier, S., Williams, L. R., Onasch, T. B., Cappa, C. D., Zhang, X., Russell, L. M., Chen, C. L., Sanchez, K. J., Worsnop, D. R., and Zhang, Q.: Influence of Emissions and Aqueous Processing on Particles Containing Black Carbon in a Polluted Urban Environment: Insights From a Soot Particle-Aerosol Mass Spectrometer, J. Geophys. Res.-Atmos., 123, 6648–6666, https://doi.org/10.1002/2017JD027851, 2018.

Corbin, J. C., Sierau, B., Gysel, M., Laborde, M., Keller, A., Kim, J., Petzold, A., Onasch, T. B., Lohmann, U., and Mensah, A. A.: Mass spectrometry of refractory black carbon particles from six sources: carbon-cluster and oxygenated ions, Atmos. Chem. Phys., 14, 2591–2603, https://doi.org/10.5194/acp-14-2591-2014, 2014.

Corbin, J. C., Lohmann, U., Sierau, B., Keller, A., Burtscher, H., and Mensah, A. A.: Black carbon surface oxidation and organic composition of beech-wood soot aerosols, Atmos. Chem. Phys., 15, 11885–11907, https://doi.org/10.5194/acp-15-11885-2015, 2015.

Cubison, M. J., Ortega, A. M., Hayes, P. L., Farmer, D. K., Day, D., Lechner, M. J., Brune, W. H., Apel, E., Diskin, G. S., Fisher, J. A., Fuelberg, H. E., Hecobian, A., Knapp, D. J., Mikoviny, T., Riemer, D., Sachse, G. W., Sessions, W., Weber, R. J., Weinheimer, A. J., Wisthaler, A., and Jimenez, J. L.: Effects of aging on organic aerosol from open biomass burning smoke in aircraft and laboratory studies, Atmos. Chem. Phys., 11, 12049–12064, https://doi.org/10.5194/acp-11-12049-2011, 2011.

Das, S., Miller, B. V., Prospero, J. M., Gaston, C. J., Royer, H. M., Blades, E., Sealy, P., and Chellam, S.: Coupling Sr-Nd-Hf Isotope Ratios and Elemental Analysis to Accurately Quantify North African Dust Contributions to $PM_{2.5}$ in a Complex Urban Atmosphere by Reducing Mineral Dust Collinearity, Environ. Sci. Technol., 56, 7729–7740, https://doi.org/10.1021/acs.est.2c01233, 2022.

DeCarlo, P. F., Kimmel, J. R., Trimborn, A., Northway, M. J., Jayne, J. T., Aiken, A. C., Gonin, M., Fuhrer, K., Horvath, T., Docherty, K. S., Worsnop, D. R., and Jimenez, J. L.: Field-deployable, high-resolution, time-of-flight aerosol mass spectrometer, Anal. Chem., 78, 8281–8289, https://doi.org/10.1021/ac061249n, 2006.

Emerson, E. W., Katich, J. M., and Farmer, D. K.: Direct Measurements of Dry and Wet Deposition of Black Carbon Over a Grassland, J. Geophys. Res.-Atmos., 123, 12277–12290, https://doi.org/10.1029/2018JD028954, 2018.

Falk, J., Korhonen, K., Malmborg, V. B., Gren, L., Eriksson, A. C., Karjalainen, P., Markkula, L., Bengtsson, P., Virtanen, A., Svenningsson, B., Pagels, J., and Kristensen, T. B.: Immersion Freezing Ability of Freshly Emitted Soot with Various Physico-Chemical Characteristics, Atmosphere, 12, 1173, https://doi.org/10.3390/atmos12091173, 2021.

Farley, R. and Zhang, Q.: TRACER-CAT laser only SP-AMS measurements, ARM archive [data set], https://doi.org/10.5439/1958716, 2023.

Fierce, L., Riemer, N., and Bond, T. C.: Toward Reduced Representation of Mixing State For Simulating Aerosol Effects on Climate, B. Am. Meteorol. Soc., 98, 971–980, https://doi.org/10.1175/BAMS-D-16-0028.1, 2017.

Fierce, L., Onasch, T. B., Cappa, C. D., Mazzoleni, C., China, S., Bhandari, J., Davidovits, P., Al Fischer, D., Helgestad, T., Lambe, A. T., Sedlacek, A. J., Smith, G. D., and Wolff, L.: Radiative absorption enhancements by black carbon controlled by particle-to-particle heterogeneity in composition, P. Natl. Acad. Sci. USA, 117, 5196–5203, https://doi.org/10.1073/pnas.1919723117, 2020.

Fofie, E. A., Donahue, N. M., and Asa-Awuku, A.: Cloud condensation nuclei activity and droplet formation of primary and secondary organic aerosol mixtures, Aerosol Sci. Tech., 52, 242–251, https://doi.org/10.1080/02786826.2017.1392480, 2018.

Fortner, E. C., Brooks, W. A., Onasch, T. B., Canagaratna, M. R., Massoli, P., Jayne, J. T., Franklin, J. P., Knighton, W. B., Wormhoudt, J., Worsnop, D. R., Kolb, C. E., and Herndon, S. C.: Particulate emissions measured during the TCEQ comprehensive flare emission study, Ind. Eng. Chem. Res., 51, 12586–12592, https://doi.org/10.1021/ie202692y, 2012.

Ge, X., Zhang, Q., Sun, Y., Ruehl, C., and Setyan, A.: Effect of aqueous-phase processing on aerosol chemistry and size distributions in Fresno, California, during wintertime, Environ. Chem., 9, 221–235, 2012a.

Ge, X., Setyan, A., Sun, Y., and Zhang, Q.: Primary and secondary organic aerosols in Fresno, California during wintertime: Results from high resolution aerosol mass spectrometry, J. Geophys. Res.-Atmos., 117, 1–15, https://doi.org/10.1029/2012JD018026, 2012b.

Gorkowski, K., Lee, J. E., Farley, R. N., Dal Porto, R., Cappa, C. D., Zhang, Q., Shawon, A. S., Benedict, K. B., Aiken, A. C., and Dubey, M. K.: Properties of Transported Dust Aerosol During TRACER, in preparation, 2024.

Gysel, M., Crosier, J., Topping, D. O., Whitehead, J. D., Bower, K. N., Cubison, M. J., Williams, P. I., Flynn, M. J., McFiggans, G. B., and Coe, H.: Closure study between chemical composition and hygroscopic growth of aerosol particles during TORCH2, Atmos. Chem. Phys., 7, 6131–6144, https://doi.org/10.5194/acp-7-6131-2007, 2007.

Healy, R. M., Evans, G. J., Murphy, M., Tritscher, T., Laborde, M., Weingartner, E., Gysel, M., Poulain, L., Kamilli, K. A., Wiedensohler, A., Connor, I. P. O., Mcgillicuddy, E., Sodeau, J. R., and Wenger, J. C.: Predicting hygroscopic growth using single particle chemical composition estimates, J. Geophys. Res.-Atmos., 119, 9567–9577, https://doi.org/10.1002/2014JD021888, 2014.

Healy, R. M., Wang, J. M., Jeong, C., Lee, A. K. Y., Willis, M. D., Jaroudi, E., Zimmerman, N., Hilker, N., Murphy, M., Eckhardt, S., Stohl, A., Abbatt, J. P. D., Wenger, J. C., and Evans, G. J.: Light-absorbing properties of ambient black carbon and brown carbon from fossil fuel and biomass burning sources, J. Geophys. Res.-Atmos., 120, 6619–6633, https://doi.org/10.1002/2015JD023382, 2015.

Hodnebrog, Ø., Myhre, G., and Samset, B.: How shorter black carbon lifetime alters its climate effect, Nat. Commun., 5, 1–7, https://doi.org/10.1038/ncomms6065, 2014.

International Maritime Organization (IMO): IMO 2020 – cleaner shipping for cleaner air, International Maritime Organization (IMO), https://www.imo.org/en/MediaCentre/PressBriefings/pages/34-IMO-2020-sulphur-limit-.aspx (last access: 24 March 2024), 2020.

IPCC: Climate Change 2021: The Physical Science Basis. Contribution of Working Group I to the Sixth Assessment Report of the Intergovernmental Panel on Climate Change, edited by: Masson-Delmotte, V., Zhai, P., Pirani, A., Connors, S. L., Péan, C., Berger, S., Caud, N., Chen, Y., Goldfarb, L., Gomis, M. I., Huang, M., Leitzell, K., Lonnoy, E., Matthews, J. B. R., Maycock, T. K., Waterfield, T., Yelekçi, O., Yu, R., and Zhou, B., Cambridge University Press, United Kingdom and New York, NY, USA, https://doi.org/10.1017/9781009157896.002, 2021.

Jahn, L. G., Jahl, L. G., Bland, G. D., Bowers, B. B., Monroe, L. W., and Sullivan, R. C.: Metallic and crustal elements in biomass-burning aerosol and ash: Prevalence, significance, and similarity to soil particles, ACS Earth Sp. Chem., 5, 136–148, https://doi.org/10.1021/acsearthspacechem.0c00191, 2021.

Lack, D. A. and Cappa, C. D.: Impact of brown and clear carbon on light absorption enhancement, single scatter albedo and absorption wavelength dependence of black carbon, Atmos. Chem. Phys., 10, 4207–4220, https://doi.org/10.5194/acp-10-4207-2010, 2010.

Lambe, A. T., Onasch, T. B., Massoli, P., Croasdale, D. R., Wright, J. P., Ahern, A. T., Williams, L. R., Worsnop, D. R., Brune, W. H., and Davidovits, P.: Laboratory studies of the chemical composition and cloud condensation nuclei (CCN) activity of secondary organic aerosol (SOA) and oxidized primary organic aerosol (OPOA), Atmos. Chem. Phys., 11, 8913–8928, https://doi.org/10.5194/acp-11-8913-2011, 2011.

Lambe, A. T., Ahern, A. T., Wright, J. P., Croasdale, D. R., Davidovits, P., and Onasch, T. B.: Oxidative aging and cloud condensation nuclei activation of laboratory combustion soot, J. Aerosol Sci., 79, 31–39, https://doi.org/10.1016/j.jaerosci.2014.10.001, 2015.

Lee, A. K. Y., Willis, M. D., Healy, R. M., Onasch, T. B., and Abbatt, J. P. D.: Mixing state of carbonaceous aerosol in an urban environment: single particle characterization using the soot particle aerosol mass spectrometer (SP-AMS), Atmos. Chem. Phys., 15, 1823–1841, https://doi.org/10.5194/acp-15-1823-2015, 2015.

Lee, A. K. Y., Willis, M. D., Healy, R. M., Wang, J. M., Jeong, C.-H., Wenger, J. C., Evans, G. J., and Abbatt, J. P. D.: Single-particle characterization of biomass burning organic aerosol (BBOA): evidence for non-uniform mixing of high molecular weight organics and potassium, Atmos. Chem. Phys., 16, 5561–5572, https://doi.org/10.5194/acp-16-5561-2016, 2016.

Lee, A. K. Y., Chen, C.-L., Liu, J., Price, D. J., Betha, R., Russell, L. M., Zhang, X., and Cappa, C. D.: Formation of secondary organic aerosol coating on black carbon particles near vehicular emissions, Atmos. Chem. Phys., 17, 15055–15067, https://doi.org/10.5194/acp-17-15055-2017, 2017.

Lee, A. K. Y., Rivellini, L. H., Chen, C. L., Liu, J., Price, D. J., Betha, R., Russell, L. M., Zhang, X., and Cappa, C. D.: Influences of Primary Emission and Secondary Coating Formation on the Particle Diversity and Mixing State of Black Carbon Particles, Environ. Sci. Technol., 53, 9429–9438, https://doi.org/10.1021/acs.est.9b03064, 2019.

Lee, J. E., Gorkowski, K., Meyer, A. G., Benedict, K. B., Aiken, A. C., and Dubey, M. K.: Wildfire Smoke Demonstrates Significant and Predictable Black Carbon Light Absorption Enhancements, Geophys. Res. Lett., 49, e2022GL099334, https://doi.org/10.1029/2022GL099334, 2022.

Levy, M. E., Zhang, R., Khalizov, A. F., Zheng, J., Collins, D. R., Glen, C. R., Wang, Y., Yu, X. Y., Luke, W., Jayne, J. T., and Olaguer, E.: Measurements of submicron aerosols in Houston, Texas during the 2009 SHARP field campaign, J. Geophys. Res.-Atmos., 118, 10518–10534, https://doi.org/10.1002/jgrd.50785, 2013.

Li, W., Wang, Y., Bernier, C., and Estes, M.: Identification of Sea Breeze Recirculation and Its Effects on Ozone in Houston, TX, During DISCOVER-AQ 2013, J. Geophys. Res.-Atmos., 125, 1–21, https://doi.org/10.1029/2020JD033165, 2020.

Liu, F., Yon, J., Fuentes, A., Lobo, P., Gregory, J., and Corbin, J. C.: Review of recent literature on the light absorption properties of black carbon: Refractive index, mass absorption cross section, and absorption function, Aerosol Sci. Tech., 54, 33–51, https://doi.org/10.1080/02786826.2019.1676878, 2020.

Liu, X., Ma, P.-L., Wang, H., Tilmes, S., Singh, B., Easter, R. C., Ghan, S. J., and Rasch, P. J.: Description and evaluation of a new four-mode version of the Modal Aerosol Module (MAM4) within version 5.3 of the Community Atmosphere Model, Geosci. Model Dev., 9, 505–522, https://doi.org/10.5194/gmd-9-505-2016, 2016.

Ma, M., Rivellini, L.-H., Kasthuriarachchi, N., Zhu, Q., Zong, Y., Yu, W., Yang, W., Kraft, M., and Lee, A. K. Y.: Effects of polyoxymethylene dimethyl ether ($PODE_n$) blended fuel on diesel engine emission: Insight from soot-particle aerosol mass spectrometry and aethalometer measurements, Atmos. Environ. X, 18, 100216, https://doi.org/10.1016/j.aeaoa.2023.100216, 2023.

Motos, G., Schmale, J., Corbin, J. C., Zanatta, M., Baltensperger, U., and Gysel-Beer, M.: Droplet activation behaviour of atmospheric black carbon particles in fog as a function of their size and mixing state, Atmos. Chem. Phys., 19, 2183–2207, https://doi.org/10.5194/acp-19-2183-2019, 2019.

Ng, N. L., Canagaratna, M. R., Jimenez, J. L., Chhabra, P. S., Seinfeld, J. H., and Worsnop, D. R.: Changes in organic aerosol composition with aging inferred from aerosol mass spectra, Atmos. Chem. Phys., 11, 6465–6474, https://doi.org/10.5194/acp-11-6465-2011, 2011.

NOAA: HYSPLIT model, NOAA Air Resources Laboratory, NOAA [code], https://www.ready.noaa.gov/HYSPLIT.php (last access: 24 March 2024), 2024.

Onasch, T. B., Trimborn, A., Fortner, E. C., Jayne, J. T., Kok, G. L., Williams, L. R., Davidovits, P., and Worsnop, D. R.: Soot particle aerosol mass spectrometer: Development, validation, and initial application, Aerosol Sci. Tech., 46, 804–817, https://doi.org/10.1080/02786826.2012.663948, 2012.

Paatero, P. and Tapper, U.: Positive matrix factorization: A non-negative factor model with optimal utilization of error estimates of data values, Environmetrics, 5, 111–126, https://doi.org/10.1002/env.3170050203, 1994.

Peng, J., Hu, M., Guo, S., Du, Z., Zheng, J., Shang, D., Zamora, M. L., Zeng, L., Shao, M., Wu, Y. S., Zheng, J., Wang, Y., Glen, C. R., Collins, D. R., Molina, M. J., and Zhang, R.: Markedly enhanced absorption and direct radiative forcing of black carbon under polluted urban environments, P. Natl. Acad. Sci. USA, 113, 4266–4271, https://doi.org/10.1073/pnas.1602310113, 2016.

Petters, M. D. and Kreidenweis, S. M.: A single parameter representation of hygroscopic growth and cloud condensation nucleus activity, Atmos. Chem. Phys., 7, 1961–1971, https://doi.org/10.5194/acp-7-1961-2007, 2007.

Popovicheva, O., Kireeva, E., Persiantseva, N., Timofeev, M., Bladt, H., Ivleva, N. P., Niessner, R., and Moldanová, J.: Microscopic characterization of individual particles from multicomponent ship exhaust, J. Environ. Monit., 14, 3101–3110, https://doi.org/10.1039/c2em30338h, 2012.

Price, D. J., Chen, C. L., Russell, L. M., Lamjiri, M. A., Betha, R., Sanchez, K., Liu, J., Lee, A. K. Y., and Cocker, D. R.: More unsaturated, cooking-type hydrocarbon-like organic aerosol particle emissions from renewable diesel compared to ultra low sulfur diesel in at-sea operations of a research vessel, Aerosol Sci. Tech., 51, 135–146, https://doi.org/10.1080/02786826.2016.1238033, 2017.

Ramanathan, V. and Carmichael, G.: Global and regional climate changes due to black carbon, Nat. Geosci., 1, 221–227, https://doi.org/10.1038/ngeo156, 2008.

Riemer, N. and West, M.: Quantifying aerosol mixing state with entropy and diversity measures, Atmos. Chem. Phys., 13, 11423–11439, https://doi.org/10.5194/acp-13-11423-2013, 2013.

Rivellini, L.-H., Adam, M. G., Kasthuriarachchi, N., and Lee, A. K. Y.: Characterization of carbonaceous aerosols in Singapore: insight from black carbon fragments and trace metal ions detected by a soot particle aerosol mass spectrometer, Atmos. Chem. Phys., 20, 5977–5993, https://doi.org/10.5194/acp-20-5977-2020, 2020.

Rivera, C., Mellqvist, J., Samuelsson, J., Lefer, B., Alvarez, S., and Patel, M. R.: Quantification of NO_2 and SO_2 emissions from the houston ship channel and texas city industrial areas during the 2006 texas air quality study, J. Geophys. Res.-Atmos., 115, 1–10, https://doi.org/10.1029/2009JD012675, 2010.

Schulze, B. C., Wallace, H. W., Bui, A. T., Flynn, J. H., Erickson, M. H., Alvarez, S., Dai, Q., Usenko, S., Sheesley, R. J., and Griffin, R. J.: The impacts of regional shipping emissions on the chemical characteristics of coastal submicron aerosols near Houston, TX, Atmos. Chem. Phys., 18, 14217–14241, https://doi.org/10.5194/acp-18-14217-2018, 2018.

Sonntag, D. B., Bailey, C. R., Fulper, C. R., and Baldauf, R. W.: Contribution of Lubricating Oil to Particulate Matter Emissions from Light-Duty Gasoline Vehicles in Kansas City, Environ. Sci. Technol., 46, 4191–4199, https://doi.org/10.1021/es203747f, 2012.

Sun, Y. L., Zhang, Q., Schwab, J. J., Yang, T., Ng, N. L., and Demerjian, K. L.: Factor analysis of combined organic and inorganic aerosol mass spectra from high resolution aerosol mass spectrometer measurements, Atmos. Chem. Phys., 12, 8537–8551, https://doi.org/10.5194/acp-12-8537-2012, 2012.

Ulbrich, I. M., Canagaratna, M. R., Zhang, Q., Worsnop, D. R., and Jimenez, J. L.: Interpretation of organic components from Positive Matrix Factorization of aerosol mass spectrometric data, Atmos. Chem. Phys., 9, 2891–2918, https://doi.org/10.5194/acp-9-2891-2009, 2009.

Ulbrich, I. M., Canagaratna, M. R., Cubison, M. J., Zhang, Q., Ng, N. L., Aiken, A. C., and Jimenez, J. L.: Three-dimensional factorization of size-resolved organic aerosol mass

spectra from Mexico City, Atmos. Meas. Tech., 5, 195–224, https://doi.org/10.5194/amt-5-195-2012, 2012.

University of Colorado: TOF-AMS software downloads, University of Colorado [code], https://cires1.colorado.edu/jimenez-group/ToFAMSResources/ToFSoftware/index.html (last access: 24 March 2024), 2024.

Wang, J., Ye, J., Liu, D., Wu, Y., Zhao, J., Xu, W., Xie, C., Shen, F., Zhang, J., Ohno, P. E., Qin, Y., Zhao, X., Martin, S. T., Lee, A. K. Y., Fu, P., Jacob, D. J., Zhang, Q., Sun, Y., Chen, M., and Ge, X.: Characterization of submicron organic particles in Beijing during summertime: comparison between SP-AMS and HR-AMS, Atmos. Chem. Phys., 20, 14091–14102, https://doi.org/10.5194/acp-20-14091-2020, 2020.

Wang, X., Ye, X., Chen, J., Wang, X., Yang, X., Fu, T.-M., Zhu, L., and Liu, C.: Direct links between hygroscopicity and mixing state of ambient aerosols: estimating particle hygroscopicity from their single-particle mass spectra, Atmos. Chem. Phys., 20, 6273–6290, https://doi.org/10.5194/acp-20-6273-2020, 2020.

Wang, Y., Ma, P. L., Peng, J., Zhang, R., Jiang, J. H., Easter, R. C., and Yung, Y. L.: Constraining Aging Processes of Black Carbon in the Community Atmosphere Model Using Environmental Chamber Measurements, J. Adv. Model. Earth Syst., 10, 2514–2526, https://doi.org/10.1029/2018MS001387, 2018.

Watson-Parris, D., Christensen, M. W., Laurenson, A., Clewley, D., Gryspeerdt, E., and Stier, P.: Shipping regulations lead to large reduction in cloud perturbations, P. Natl. Acad. Sci. USA, 119, e2206885119, https://doi.org/10.1073/pnas.2206885119, 2022.

Williams, L. R., Gonzalez, L. A., Peck, J., Trimborn, D., McInnis, J., Farrar, M. R., Moore, K. D., Jayne, J. T., Robinson, W. A., Lewis, D. K., Onasch, T. B., Canagaratna, M. R., Trimborn, A., Timko, M. T., Magoon, G., Deng, R., Tang, D., de la Rosa Blanco, E., Prévôt, A. S. H., Smith, K. A., and Worsnop, D. R.: Characterization of an aerodynamic lens for transmitting particles greater than 1 micrometer in diameter into the Aerodyne aerosol mass spectrometer, Atmos. Meas. Tech., 6, 3271–3280, https://doi.org/10.5194/amt-6-3271-2013, 2013.

Willis, M. D., Lee, A. K. Y., Onasch, T. B., Fortner, E. C., Williams, L. R., Lambe, A. T., Worsnop, D. R., and Abbatt, J. P. D.: Collection efficiency of the soot-particle aerosol mass spectrometer (SP-AMS) for internally mixed particulate black carbon, Atmos. Meas. Tech., 7, 4507–4516, https://doi.org/10.5194/amt-7-4507-2014, 2014.

Willis, M. D., Healy, R. M., Riemer, N., West, M., Wang, J. M., Jeong, C.-H., Wenger, J. C., Evans, G. J., Abbatt, J. P. D., and Lee, A. K. Y.: Quantification of black carbon mixing state from traffic: implications for aerosol optical properties, Atmos. Chem. Phys., 16, 4693–4706, https://doi.org/10.5194/acp-16-4693-2016, 2016.

Willis, M. D., Bozem, H., Kunkel, D., Lee, A. K. Y., Schulz, H., Burkart, J., Aliabadi, A. A., Herber, A. B., Leaitch, W. R., and Abbatt, J. P. D.: Aircraft-based measurements of High Arctic springtime aerosol show evidence for vertically varying sources, transport and composition, Atmos. Chem. Phys., 19, 57–76, https://doi.org/10.5194/acp-19-57-2019, 2019.

Worton, D. R., Isaacman, G., Gentner, D. R., Dallmann, T. R., Chan, A. W. H., Ruehl, C., Kirchstetter, T. W., Wilson, K. R., Harley, R. A., and Goldstein, A. H.: Lubricating Oil Dominates Primary Organic Aerosol Emissions from Motor Vehicles, Environ. Sci. Technol., 48, 3698–3706, https://doi.org/10.1021/es405375j, 2014.

Wu, Y., Liu, D., Wang, J., Shen, F., Chen, Y., Cui, S., Ge, S., Wu, Y., Chen, M., and Ge, X.: Characterization of Size-Resolved Hygroscopicity of Black Carbon-Containing Particle in Urban Environment, Environ. Sci. Technol., 53, 14212–14221, https://doi.org/10.1021/acs.est.9b05546, 2019.

Xie, C., Xu, W., Wang, J., Liu, D., Ge, X., Zhang, Q., Wang, Q., Du, W., Zhao, J., Zhou, W., Li, J., Fu, P., Wang, Z., Worsnop, D., and Sun, Y.: Light absorption enhancement of black carbon in urban Beijing in summer, Atmos. Environ., 213, 499–504, https://doi.org/10.1016/j.atmosenv.2019.06.041, 2019.

Yang, Y., Fu, Y., Lin, Q., Jiang, F., Lian, X., Li, L., Wang, Z., Zhang, G., Bi, X., Wang, X., and Sheng, G.: Recent advances in quantifying wet scavenging efficiency of black carbon aerosol, Atmosphere, 10, 1–19, https://doi.org/10.3390/atmos10040175, 2019.

Ye, Q., Gu, P., Li, H. Z., Robinson, E. S., Lipsky, E., Kaltsonoudis, C., Lee, A. K. Y., Apte, J. S., Robinson, A. L., Sullivan, R. C., Presto, A. A., and Donahue, N. M.: Spatial Variability of Sources and Mixing State of Atmospheric Particles in a Metropolitan Area, Environ. Sci. Technol., 52, 6807–6815, https://doi.org/10.1021/acs.est.8b01011, 2018.

Yoon, S., Usenko, S., and Sheesley, R. J.: Fine and Coarse Carbonaceous Aerosol in Houston, TX, during DISCOVER-AQ, Atmosphere, 11, 1–14, https://doi.org/10.3390/ATMOS11050482, 2020.

Young, D. E., Kim, H., Parworth, C., Zhou, S., Zhang, X., Cappa, C. D., Seco, R., Kim, S., and Zhang, Q.: Influences of emission sources and meteorology on aerosol chemistry in a polluted urban environment: results from DISCOVER-AQ California, Atmos. Chem. Phys., 16, 5427–5451, https://doi.org/10.5194/acp-16-5427-2016, 2016.

Yu, C., Pasternak, D., Lee, J., Yang, M., Bell, T., Bower, K., Wu, H., Liu, D., Reed, C., Bauguitte, S., Cliff, S., Trembath, J., Coe, H., and Allan, J. D.: Characterizing the Particle Composition and Cloud Condensation Nuclei from Shipping Emission in Western Europe, Environ. Sci. Technol., 54, 15604–15612, https://doi.org/10.1021/acs.est.0c04039, 2020.

Zhang, Q., Worsnop, D. R., Canagaratna, M. R., and Jimenez, J. L.: Hydrocarbon-like and oxygenated organic aerosols in Pittsburgh: insights into sources and processes of organic aerosols, Atmos. Chem. Phys., 5, 3289–3311, https://doi.org/10.5194/acp-5-3289-2005, 2005.

Zuberi, B., Johnson, K. S., Aleks, G. K., Molina, L. T., Molina, M. J., and Laskin, A.: Hydrophilic properties of aged soot, Geophys. Res. Lett., 32, 2–5, https://doi.org/10.1029/2004GL021496, 2005.